Research article

Elucidation of structural, electromagnetic, and optical properties of Cu–Mg ferrite nanoparticles

Sushen Chandra Devsharma [a,b], Md. Lutfor Rahman [a,*], Md. Jakir Hossain [b], Bristy Biswas [a], Md. Farid Ahmed [a], Nahid Sharmin [a]

[a] Institute of Glass and Ceramic Research and Testing (IGCRT), Bangladesh Council of Scientific and Industrial Research (BCSIR), Dhanmondi, Dhaka-1205, Bangladesh
[b] Department of Chemistry, Begum Rokeya University, Rangpur, Bangladesh

A R T I C L E   I N F O

A B S T R A C T

Copper doped magnesium ferrite, $Mg_{1-x}Cu_xFe_2O_4$(x = 0.0–1.0) nanomaterials were synthesized via. sol-gel method sintered at 600 °C for 2 h. The synthesized materials were characterized using modern sophisticated techniques viz. X-ray diffraction (XRD), Scanning electron microscopy (SEM), Transmission electron microscopy, Energy dispersive x-ray spectroscopy (EDS), Vibrating sample magnetometer, UV–visible diffuse reflectance spectra and Impedance analyzer. XRD analysis revealed that all the samples were single phase cubic spinel structure with Fd3m space group and investigated the change in structural parameters with copper concentration. The average crystallite size in the range of 11–23 nm and lattice parameters decrease with increasing Cu doping, due to the cationic distribution and ionic radius. The SEM images show the agglomeration of the particles with spherical like shape and elemental percentage were obtained from EDX. The saturation magnetization showed an increasing trend with increasing Cu concentration at a certain level and then decreases due to the rearrangement of cations at tetrahedral and octahedral sites. The Coercivity, Retentivity and magnetic crystalline anisotropy increase with changing dopant concentration. The magnetic measurements showed enhanced saturation magnetization at certain level (28.96emu/gm) and increase in coercivity up to 1102 Oe with changing dopant concentration. The estimated band gap energy is found to increase with Cu content. The dielectric constant, dielectric loss and impedance show normal behavior of ferrite. The frequency dependent dielectric constant decrease and tan delta shows a relaxation behavior at low frequencies. The synthesized nano Mg–Cu nanoparticles will be applied as humidity sensor, gas sensor, microwave devices and photocatalyst.

1. Introduction

Nanocrystalline spinel ferrites have recently garnered great attention due to their smart outlines of chemical constituents and crystal system with acceptable qualities. A wide number of applications, including those in the industries of electrical and electronic, satellite and microwave communication technologies, electronic recording system, radio frequency devices and biomedicine, are impacted by spinel ferrites [1–5]. It is also used as a magnetic materials, semiconductors, pigments, catalysts, and refractories [6].

---

* Corresponding author.
E-mail addresses: lutforrahman@bcsir.gov.bd, lutforju33@yahoo.com, lutforju33@gmail.com (Md.L. Rahman).

Depending on its structural compositions, calcination temperature, fabrication process and cationic distribution cubic spinel ferrite has both electric and magnetic properties [1]. High surface to volume ratio of nanomaterials has improved their physical and chemical characteristics [7].Compared to pure metals, spinel ferrites have superior electromagnetic performance over a wide frequency range, making them desirable magnetic and electric materials [8]. Furthermore, nanoscopic doped or substituted spinel ferrite has demonstrated unexpected new features such as large surface area, superparamagnetic nature, and biocompatibility [9,10]. As a result, extensive efforts are being made in order to advance investigate nanoscale Spinel ferrite for a variety of uses including ferrofluid, devices for magnetic data storage, environmental pollution control (catalyst), contrast agents in disease imaging, targeted medication delivery, purifying of water, and so on [11].Compounds with the general formula AB_2O_4 are known as spinel ferrites. In these compounds, the A site is tetrahedrally coordinated and filled by divalent cations (A = Ni, Cu, Zn, Co, Mg, Mn etc.) while the B site is octahedrally coordinated and occupied by the trivalent Fe^{3+} ion [8]. Magnesium-copper ferrites are n-type semiconducting materials of the ceramic type that are soft magnetic [2,4,9,12]. Cu substitution magnesium ferrite can have a significant impact on structural, morphological, and dielectric characteristics. That's why they have a low magnetic losses and high magnetic permeability, which makes them a common component of electrical and magnetic devices [8,13]. Due to its elevated resistance and low eddy currents, magnesium-copper ferrite is one of the most adaptable ferrites [7,13]. Copper doped magnesium ferrites are partly inverted spinel ferrites in which Fe^{3+} ions are rearranged into the octahedral and tetrahedral configurations that already exist [2,9]. It is a partially inverse spinel, and the degree of inversion depends on the sample's microstructure, thermal history, and preparative factors. Because of their insulating and soft magnetic qualities. $MgFe_2O_4$ and $CuFe_2O_4$ NPs are non-toxic, have high environmental stability, are biocompatible, and have diverse physicochemical features [5,14]. The soft magnetic, low magneto crystalline anisotropy, and optimal heating efficiency performance of $MgFe_2O_4$ and $CuFe_2O_4$ nanoparticles (NPs) make them important mediators for magnetic hyperthermia (MH) use in comparison to cobalt and nickel ferrite NPs (cancer treatment) [5]. The widespread usage of magnesium and copper ferrite in high density storage medium, heterogeneous catalysis, sensors, transformer core, magnetic technologies and anode materials for lithium-ion batteries and photoelectric characteristics has drawn particular attention to these ferrites [4,13,15–17]. For fabricating ferrites of various sizes and shapes, several synthesis processes, such as solid-state reactions, sono-chemical emulsification, reverse micelle technique, co-precipitation, hydrothermal, sol-gel, and ball milling have been developed over time [1,4,9,18–20]. Therefore, an attempt has been made to synthesize copper-doped magnesium ferrite using the sol-gel method. The sol-gel auto combustion technology proposed in this study seems to be a pledging choice due to its simplicity and control over product quality. The sol-gel approach, which produces nanoparticles with a high surface area and strong chemical homogeneity at lower temperatures, stands out as one of the most effective synthesis methods. Additionally, the process is incredibly easy and economical [9].

A few researches have been carried out on Cu–Mg ferrites to explore the effect of composition change on different properties of ferrites. A. Poddar et al. has synthesized copper doped magnesium ferrite (Mg1-xCuxFe2O4, x = 0.0–0.5) following standard solid state two step sintering ceramic method and found that the microstructure, magnetic properties strongly dependent on Cu content as well as on cooling rate [2]. E. Ateia et al. has synthesized Cu–Mg ferrites (Mg1-xCuxFe2O4, where $0.0 \leq x \leq 1.0$) through solid state method by pelletizing with high pressure and sintering at 1150 °C for 15 h with pre-sintering at 800 °C for 10 h and explored the electrical properties as well as initial permeability for low frequency application [21]. T. Kiseleva et al. has prepared bulk copper doped magnesium ferrites of micron sizes following conventional ceramic method at 1200 °C and observed that the synthesized materials are soft magnetic in nature in which the magnetic properties including coercivity, magnetic hyperfine interaction strongly dependent on particle size, domain state and cation distribution [22]. A. Balamurugan et al. have studied the effect of natural fuel lemon juice and heating temperature on structural, electromagnetic and humidity sensing properties of sol-gel synthesized magnesium substituted copper ferrite ($Mg_{0.4}Cu_{0.6}Fe_2O_4$) nanoparticles. So, there is no sequential investigation of different characteristics of copper doped magnesium ferrite nanoparticles [23]. L. Rajadurai et al. has prepared Mg1-xCuxFe2O4 (x = 0.0, 0.1, 0.3, and 0.5) nanoparticles by microwave assisted combustion technique using ʟ-arginine as fuel and studied their photocatalytic efficiency with mechanism for $Mg_{0.7}Cu_{0.3}Fe_2O_4$ nanoparticles [24].

The current work therefore focuses on a novel approach utilizing the sol-gel method for the synthesis of copper-doped magnesium ferrite $Mg_{1-x}Cu_xFe_2O_4$ (x = 0.00, 0.25, 0.50, 0.75, and 1.00) nanoparticles. The calcination temperature employed was 600 °C, allowing for an in-depth exploration of the material's structural, morphological, magnetic, electrical, and optical properties in a systematic manner. It effectively controls particle size and purity, resulting in desired nanoparticle qualities. Various characterization techniques, including Thermogravimetric analysis (TGA), X-ray diffraction (XRD), scanning electron microscopy (SEM), Transmission electron microscopy (TEM), energy dispersive X-ray spectroscopy (EDX), UV–Visible diffuse reflectance spectra (DRS), vibrating sample magnetometer (VSM), and impedance analyzer were utilized, and the findings are reported here. The synthesized nano Mg–Cu nanoparticles will be applied as humidity sensor, gas sensor, microwave devices and photocatalyst.

2. Experimental

2.1. Materials & method

Sol-gel auto combustion procedures were used to generate nanoparticles having the chemical formula $Mg_{1-x}Cu_xFe_2O_4$ (x = 0.00, 0.25, 0.50, 0.75, and 1.00). Firstly, stoichiometrically precise 0.5 M solutions of highly pure magnesium nitrate [$Mg(NO_3)_2.6H_2O$] (Merck, Germany), ferric nitrate [$Fe(NO_3)_3.9H_2O$] (Merck, Germany), and copper nitrate [$Cu(NO_3)_2.3H_2O$] (Merck, Germany) salts were separately prepared by dissolving them in deionized water. These salts solutions of were blended in a 1000 ml beaker and vigorously stirred for 30 min at room temperature. Subsequently, citric acid ($C_6H_8O_7.H_2O$) solution (0.5 M) was added to the solution in a molar ratio of 1:2 with respect to the cations. After that, 25 % ammonia solution was gently added until the pH was seven. As a

chelating agent citric acid was utilized [25]. At room temperature, the mixing process continues to ensure a well-mixed solution and a proper distribution of the components. The mixture was then heated to 80 °C until it formed a moist viscous porous brownish gel. The heating process was continued until completed the aging of gel for a few minutes. The produced gel was heated to 100 °C and obtained dried mass or ash. As prepared materials were collected and ground. The pure and substituted samples were then sintered for 2 h in a muffle furnace at 600 °C. The detailed synthesis procedures are presented in Fig. 1. The synthesized materials have been indicated as S1 when x = 0.00 for $MgFe_2O_4$(pure), S2 when x = 0.25 ($Mg_{0.75}Cu_{0.25}Fe_2O_4$), S3 when x = 0.50 ($Mg_{0.5}Cu_{0.5}Fe_2O_4$), S4 when x = 0.75 ($Mg_{0.25}Cu_{0.75}Fe_2O_4$), and finally, S5 when x = 1.00 (pure $CuFe_2O_4$).

2.2. Characterizations

Crystallinity and phase identification of the Copper doped $MgFe_2O_4$ are studied by X-ray Diffractometer (ARL Equinox-1000, Thermo Fisher Scientific Incorporation, USA) with copper K-alpha radiation(λ = 1.54056 Å) in the range of theta value 10°–80°. Elemental percentage of the materials' composition was determined by Energy Dispersive X-ray spectroscopy and surface morphology of the samples were directly examined by the Scanning Electron Microscopy (SEM Model; MA15 VP-SEM, Carl Zeiss Evo, UK). The average grain size was measured from about 60 grains randomly using Image-J software. Optical properties of the synthesized Cu-doped magnesium ferrites were measured by UV–Visible NIR (Model: LAMDA 1050+, PerkinElmer, UK) through recorded diffuse reflectance in the range 380–780 nm. Fourier transform infrared spectra (FTIR) were recorded using (Model-IRAffinity-1S, MIRacle 10, Shimadzu Japan) FTIR spectrometer utilizing KBr as a binder for analyzing the wave number varies from 400 to 4000 cm^{-1}. Room temperature dielectric and permeability measurements were carried out through the Impedance analyzer (Model-65120B, Wayne Kerr Electronics, UK). To make pellets for dielectric study, Cu doped Magnesium ferrite powder samples were combined with 10 % aqueous polyvinyl alcohol (PVA) solution. After drying, the mixture was then compacted to form a 13-mm-diameter circular pellet. Polyvinyl alcohol (PVA) was used as an excellent binder in nanoparticles. To remove the PVA influence on the ferrite components, the pellets were sintered at 400 °C for 30 min with a heating rate 1.0 °C/min [26]. Eventually, the pellets were put between two conductive plates of dielectric measurement fixture (model: 1 J1020) and the frequency dependent capacitance, impedance, resistance, conductivity and phase angle were measured to determine the dielectric and electric properties of the pellets with a precision impedance analyzer in the range of 100 Hz to 20 MHz. Magnetic measurements were carried out using a vibrating sample magnetometer (VSM: Model-8604, Lakeshore USA) at ambient temperature (300K) with an employed field range from −15 to +15 kOe.

3. Result and discussions

3.1. TGA-DSC analyses

Fig. 2 depicts the TGA and DSC curves of the intermediate of pure magnesium ferrite (S1) at temperatures ranging from 25 to 1000 °C. The figure depicts the precursor's decomposition and the synthesis of magnesium ferrite nanoparticles. The TGA curve shows that as the temperature rises, the distinct zones of weight loss are detected. The weight loss in the range between 50 °C and 170 °C might be attributable to coordinated water evaporation [27]. The major weight loss in this region was happened at about 95 °C as depicted by the DTG curve which is endothermic in nature as indicated by the DSC graph and the coordinated moisture might be
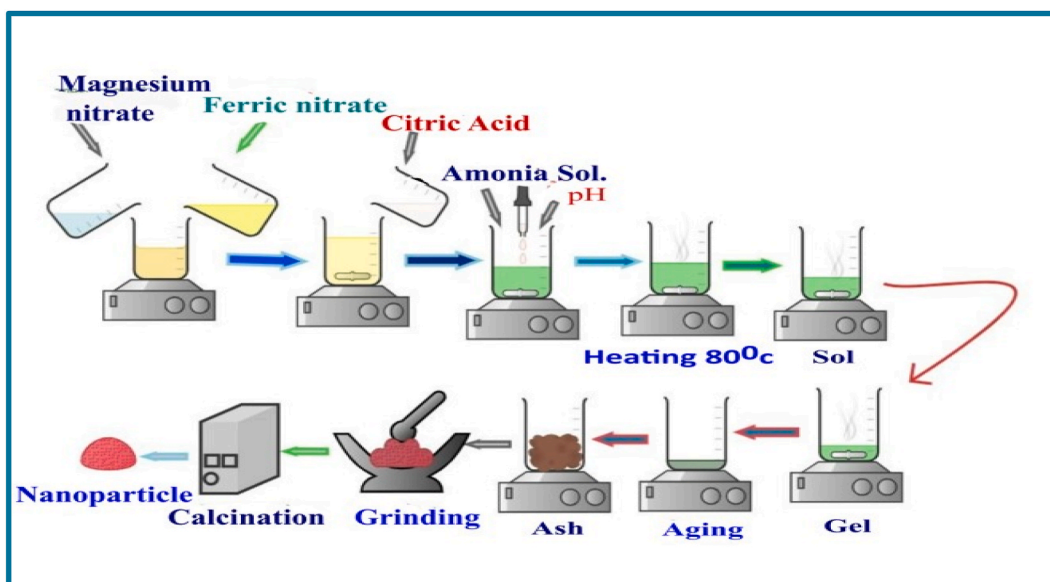

Fig. 1. Schematic diagram for the preparation of $Mg_{1-x}Cu_xFe_2O_4$ nanoparticles.
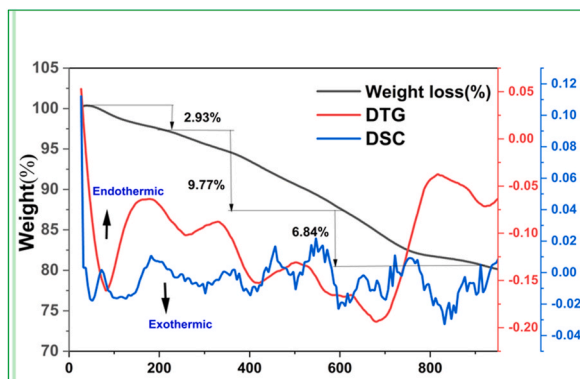
Fig. 2. TGA-DSC graph for the intermediate of magnesium ferrite.

responsible for the endothermic peak. The major weight loss was observed in the broad region from 170 °C 750 °C in which several endothermic peaks at about 180 °C, 385 °C, 470 °C, 580 °C and 750 °C were found in the DSC curve. These weight losses were due to the degradation of metal-organic complex and evaporation of CO_2 and H_2O, autocatalytic oxidation-reduction breakdown between NH_4^+, NO_3^- and citric acid [28]. At temperatures exceeding 750 °C, no more weight loss was detected, implying complete annihilation of organic components and the creation of nanocrystalline magnesium ferrite [29,30]. The altitude part over 750 °C clearly shows spinel formation [31,32]

3.2. X-ray diffraction (XRD) analysis

Fig. 3 displays the X-ray diffraction (XRD) patterns for the series of samples of sintered at 600 °C for 120min. A single-phase cubic Spinel structure with no extra lines corresponding to any other crystallographic phase was formed using an X-ray phase analysis. The XRD patterns for all $Mg_{1-x}Cu_xFe_2O_4$ samples with (h k l) values that are in accordance with the diffraction peaks at 2θ values of 18.32°, 30.07°, 35.47°, 43.04°, 53.51°, 56.99°, 62.57°, 79.99°, and 89.67° of the corresponding to the hkl planes (111), (220), (311), (400), (422), (511), (440), (444), and (731). Similar XRD pattern was reported Rammaprasad.et al. [33] and Yadav R et al. [34].The 18.32°, 79.99°, and 89.67° peak corresponds to the (111),(444),(731) plane in spinel ferrite's cubic crystal structure also reveals the presence of this particular crystallographic plane in the copper doped magnesium ferrite NPs. The XRD pattern of $MgFe_2O_4$ and Cu-doped $MgFe_2O_4$ NPs are related to the cubic inverse spinel phase and space group of Fd_3 m. Peaks correspond to an indexed sequence of reference: 88–1936 for magnesium ferrite and 77-0010 for copper ferrite [2,35,36]. The study of XRD patterns revealed that the examined Mg–Cu ferrites samples have a spinel cubic structure with a single phase [2,37]. The estimate crystallite size of the samples is determined using the Debye-Scherrer formula from the diffraction peak of the (311) plane in the XRD profile [18,35].

3.2.1. Measurements of crystallite size and lattice strain

*3.2.1.1. The **wilson approach** and the **Debye-Scherrer technique** are two methods that can be used to compute lattice strain and crystallite size.* The Scherer approach is the most efficient and straightforward way. The crystallite size is calculated by using the full width at half maximum (FWHM) value [38,39]. The Debye-Scherrer method, which is based on peak widening, the limited crystallite size, strain, and flaws of variation from perfect crystallinity can all contribute to the broadening of the line diffraction pattern. Using Eq. (1), the
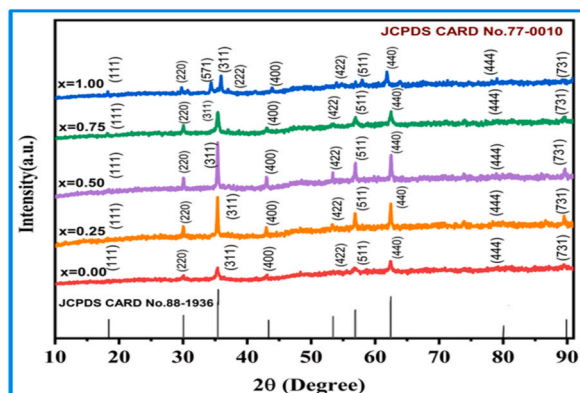

Fig. 3. X-ray diffraction patterns of $Mg_{1-x}Cu_xFe_2O_4$ with x = 0.25, 0.5, 0.75 and 1.00) nanoparticles.

estimate crystallite size is measured using the full width at half maximum (FWHM) value of the tallest peak [14,38,40].

$$D_{D-S} = \frac{K\lambda}{\beta \cos \Theta}$$ (1)

Where D_{D-S} is the crystallite size, λ is the x-ray wavelength (1.54056) for Cu-Kα radiation, K is the shape factor (here, K equal to 0.96 is used for computation), θ is the diffraction angle, and β_D is the full width at half maximum (FWHM) [3,14,41]. Based on the relation (1), size broadening is independent of the order of a reflection. D_{D-S} indicates the crystallite size, the form factor by k (k = 0.96), Wavelength of X-ray $\lambda = 0.154056$ nm for Cu-Kα radiation, the FWHM of the most intense peak identified by β_D can be manifested by reorganizing Eq. (1) we get Eq. (2)

$$\beta_D = \frac{K\lambda}{D_{D-SCOS\theta}}$$ (2)

The lattice strain in the powder sample is caused by crystal imperfection and distortion. Crystal imperfection, malformities, and lattice discrepancy are accountable for lattice strain in powder nanoparticles, that are described using the Stokes and Wilson correlation as Eq (3).

$$\varepsilon = \frac{\beta strain}{4 \tan \theta}$$ (3)

Here, the integral width for the effects of strains is represented by βstrain, whereas ε represents the lattice strain.

3.2.1.2. Halder-Wagner method. The XRD peak has neither a Lorentzian nor a Gaussian function, since the XRD peak region correlates well with the Gaussian function, but its tail drops off too rapidly without matching [38,42]. In contrast, the profile's tails fit quite well with the Lorentz function, however this does not suit the XRD peak region [38,40]. To address this issue, the Halder-Wagner method is utilized, which is based on the premise that widening of the peak is a symmetric Voigt function, since it is a convolution of Lorentzian and Gaussian functions [42]. By using (β_{hkl}) value and planar spacing (d_{hkl}) from X-ray diffraction analysis using H–W method, the specifics of crystallite size(D_{H-W}) and lattice strain(ε_{H-W}) were found. The H–W figure suggests an alternative equation with width that is integral, β^* in Eq. (5) of the mutual lattice point, and in Eq. (6) d* for interplanar spacing [14]. [43].

$$\left(\frac{\beta^*}{d^*}\right)^2 = \frac{K\beta^*}{D_{H-W}}(d^*)^2 + (2\varepsilon_{H-W})^2$$ (4)

Where, $\beta^* = \frac{\beta \cos \theta}{\lambda}$ (5)
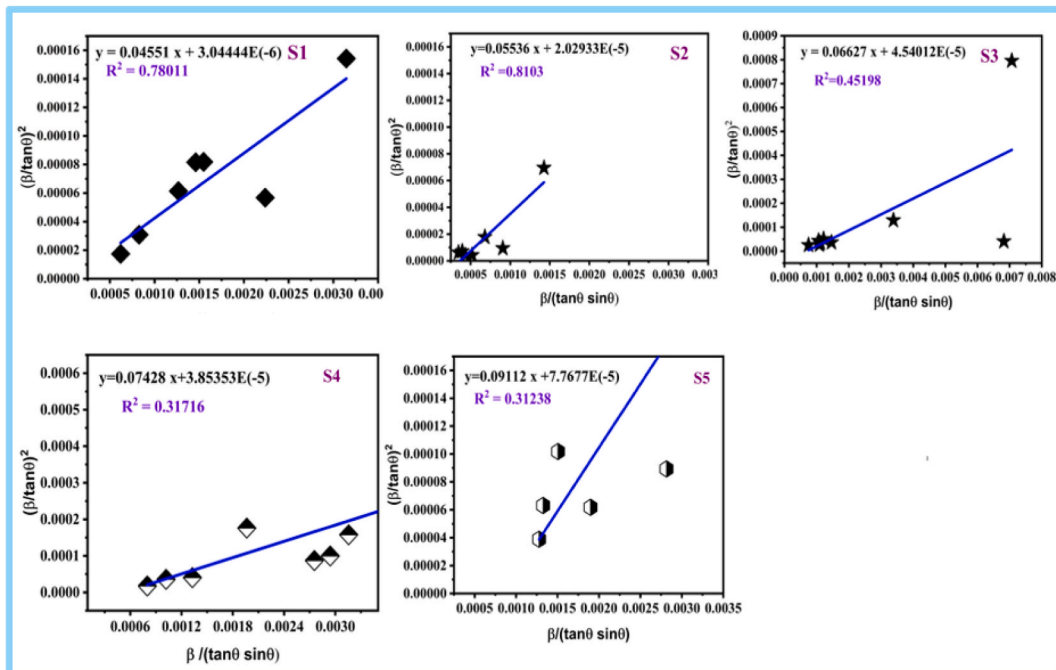

Fig. 4. H–W plot of (Mg$_{1-x}$Cu$_x$Fe$_2$O$_4$ x = 0.0, 0.25, 0.5, 0.75 and 1.00) nanomaterial.

$$d^* = \frac{2 \sin \theta}{\lambda} \tag{6}$$

By inserting this value of β^* and d* into Eq. (4),

$$\left(\frac{\cos \theta}{\sin \theta}\right)^2 = \frac{K \lambda \beta \cos \theta}{D_{H-W} \sin^2 \theta} + 16\varepsilon_{H-W}^2 \tag{7}$$

Eq. (7) can be written was

$$\left(\frac{\beta}{\tan \theta}\right)^2 = \frac{k \lambda \beta \cos \Theta}{D_{H-W} \sin^2 \theta} + 16\varepsilon_{H-W}^2 \tag{8}$$

Eq. (7) as like as $y = mx + c$, where slop is $k \lambda/D_{H-W}$ and intercept $16\varepsilon_{H-W}^2$. In Halder-Wagner method, $y=(\beta/\tan\Theta)$ [2] was plotted against $x = \beta \cos\Theta/\sin$ [2]Θ as shown in Fig. 4 and Eq. (8) The H–W plot also demonstrated that cos has a linear connection with $\sin\theta$ [42,44,45]. Positive slopes in fitted curves indicate the materials' tensile strain. The average crystallite size (D) of Mg-doped N NPs was determined based on intercept values from fitted linear lines utilizing the $(k\lambda/D)$ relation [46–48]. The straight line obtained from the data accorded size of crystallites and lattice Sstrain were determined from the slope and intercept respecttively and shown in Table 1 Using H–W method the plotted straight lines are moderately fitted, as the value of the coefficient of correlation R^2 is 0.78011, 0.81030, 0.45198, 0.31716, 0.31238 for the samples of S1, S2, S3, S4 and S5.

3.2.1.3. Size-strain plot (SSP) method. The Halder-Wagner approach takes into account peak broadening as a function of diffraction angle (2θ), which is thought to depict a combined impact of strain and size associated peak broadening. However, there are models that deal with peak profile analysis. One such approach is the Size-Strain plot (SSP), which implies that the XRD peak profile is a combination between Lorentzian and Gaussian features, with size broadened XRD profiles labeled as Lorentz functions and strain broadened profiles labeled as Gaussian functions. As a result, SSP overall broadening may be states as $\left(\beta_{hkl=\beta_L+\beta_G}\right)$ [14,38,42]

Where L and G are the Lorentz and Gaussian function peak broadenings, respectively. Moreover, the SSP method always produces a robust result for isotropic broadening because it tends to favor low angle reflections, where accuracy and precision are higher, above higher angle reflections. This is due to the decreased quality of XRD data at higher angles, and peaks are often substantially overlapped at higher diffraction angles [14,38,41]. In size-strain plot (SSP) evaluation, the Lorentzian function defines crystallite size, and the Gaussian function explains lattice strain. As a result, the SSP calculation is carried out using **Eq. (9)** shown below.

$$(d\beta \cos \theta)^2 = \frac{K(d^2\beta \cos \theta)}{D_{SSP}} + \left(\frac{\varepsilon_{SSP}}{2}\right)^2 \tag{9}$$

Table 1 provides the approximated crystallite size and apparent lattice strain depending on the slope and intercept of the linear extrapolation data by plotting $(d\beta\cos\Theta)$ [2] vs. $d^2\beta\cos\Theta$ as shown in Fig. 5.

The straight lines displayed using the SSP approach are the best match, with R^2 values of 0.69846, 0.92319, 0.96056, 0.36623 and 0.87521 for S1, S2, S3, S4, S5, respectively. Since the data more closely fits in this way, the SSP methodology offers more precise findings than the H–W plots, with all points of considerable intensity reaching linear adaptation. Therefore, the SSP technique is the most efficient [14,44]. Table No.1 displays the data for crystallite size (D_{D-S}) and strain (ε).

It has been shown that the crystallite size increases from 20.55 to 11.19 nm with increasing Cu content (x = 0.0 to 0.5) and afterwards decreases for (x = 0.75 and 1.00). The reason for first increase in crystallite size is incorporation of larger Cu^{2+} ion and further crystallite size decreases may be due to the orientation of the cations in the spinel crystal system. The strain in the $MgFe2O4$ lattice is caused by the introduction of Cu^{2+} ions by substitution or interstitial interactions. Replacing Mg^{2+} ions with Cu^{2+} ions in the $MgFe_2O_4$ host crystal structure causes lattice strain, disorder, and dislocations due to greater ionic radius of Cu^{2+} ion (76 p.m.) compared to Mg^{2+}'s (71 p.m.) [46–48]. Similar findings were reported by S. Manjura Hoque et al. [2] and M. A. Gabal et al.

3.2.2. Determination of various microstructural parameters

Dislocation line length in a unit volume of crystalline material may be used to calculate dislocation density(δ) using Eq. (10)

$$\delta = \frac{1}{D^2} \tag{10}$$

Table 1
Crystallite size and lattice strain of the $Mg_{1-X}Cu_XFe_2O_4$ (X = 0.0,0.25,0.5, 0.75 and 1.00) NPs by Debye-Scherrer, Halder-Wagner, and size-strain plot.

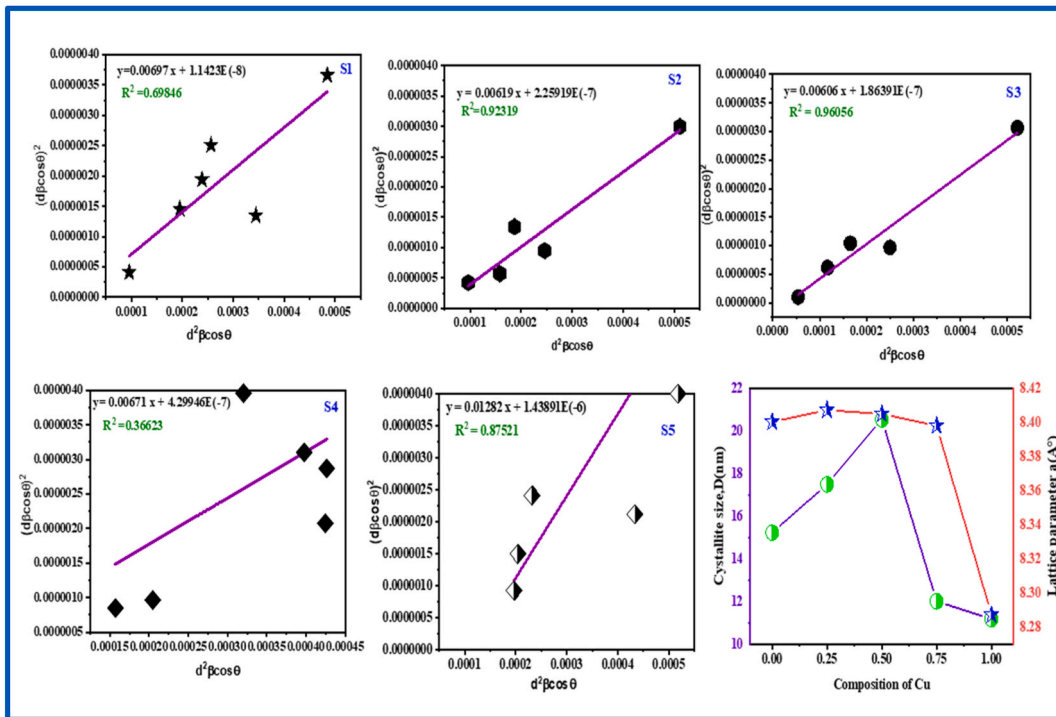| Sample ID	D-S and Wilson Method		H–W plot		SSP technique	
	DD-S(nm)	Strain $\varepsilon_w \times 10^{-3}$	D_{H-W}(nm)	$\varepsilon_w \times 10^{-3}$	D_{SSP} (nm)	$\varepsilon_w \times 10^{-4}$
S1	15.25	1.47	21.97	3.48	19.89	2.13
S2	17.51	2.71	18.06	9.00	22.39	9.50
S3	20.55	3.43	15.08	13.4	22.87	8.63
S4	12.02	2.40	13.06	12.42	20.66	13.11
S5	11.19	6.38	10.97	17.6	10.81	23.91

Fig. 5. Size strain plot & variations of lattice parameter and crystallite size of $Mg_{1-x}Cu_xFe_2O_4$ nanomaterials.

The nanoparticles lattice constant was computed using Eqs. (11) and (12). Here, "d" denotes the interplanar distance and "n" signifies the order of diffraction, which is typically equal to 1.0 according to Braggs Law [14].

$$2dsin\theta = n\lambda \tag{11}$$

$$d = \frac{n\lambda}{2\,sin\,\Theta}$$

$$a = d\sqrt{h^2 + k^2 + l^2} \tag{12}$$

The refractor plane Miller indices are h, k, and l, and the lattice constant is a. The cube of the lattice constant "a" equals the cell volume, as described in Eq. (13) Table 2 for Cu-doped magnesium ferrite (x = 0.0, 0.25, 0.5, 0.75, and 1.0), and other microstructural properties are observed.

$$V = a^3 \tag{13}$$

According to Table 2, dislocation density rises with increasing Cu^{2+} concentration, peaking at (x = 1.0) because copper has a larger atomic weight than magnesium. The dislocation density of a material is the number of dislocations per unit volume or unit area, which provides information on the material's mechanical characteristics and deformation behavior. Higher dislocation densities frequently suggest increased flexibility and deformation capabilities in metals and crystalline materials. The density of the sample is determined to be lower without Cu doping (x = 0.0) than with Cu^{2+} doping [49]. As the content of Cu increases, the lattice constantly drops (Table 2). This might be since Cu^{2+} ions (0.73) are higher than Mg^{2+} ions (0.71). Cu^{2+} inclusion in the ferrite at the detriment of Mg^{2+} is estimated to diminish the lattice constant [9,14,37]. Also, the lattice constant is approximately to the theoretical lattice constant of

Table 2
The impact of Cu substitution on a variety of microstructural parameters.

Sample Id	Dislocation	density, δ(lines/m^2)		Lattice constant(Å)	Cell Volume (Å)
	D-S method	H–W plot	SSP technique		
S1	42.98	20.71	25.27	8.4005	592.80
S2	32.61	30.65	19.94	8.4074	594.27
S3	23.67	43.97	19.12	8.4051	573.78
S4	69.21	58.62	23.42	8.3982	592.32
S5	79.86	83.09	85.57	8.2873	569.16

magnesium ferrite which is 8.426 Å[50]. After analyzing the XRD data, structural investigations indicated that all the sol-gel samples are single phases of face-centered cubic (FCC) spinel with a space group Fd-3m symmetry structure.

3.3. FTIR analysis

The spectrum of $Mg_{0.5}Cu_{0.5}Fe_2O_4$ sample in the 4000-400 cm^{-1} regions was recorded using a Fourier Transform Infrared Spectrometer as shown in Fig. 6 and the spectrum 1000-400 cm^{-1} regions is visualized in the inset of Fig. 6. The observations indicate that multiple peaks bear the responsibility for distinct functional groups exist in the 3600-1200 cm^{-1} region. A modest broad peak at 3426 cm^{-1} revealed the presence of an O–H group, while C–H bending may be found in the 850-1200 cm^{-1} region [9]. The first band(ν1), discovered between 600 and 550 cm^{-1}, was owing to the fundamental stretching vibrations of metal-oxygen bond at the tetrahedral site (M_{Tetra}-O), whereas the second band (ν2), identified between 450 and 400 cm^{-1}, corresponded to stretching vibrations of metal-oxygen bond at the octahedral site (M_{Octa}–O) [51]. The stretching mode of O–H and H–O–H bending vibration of free or absorbed water was linked to the projecting bands about 3400 cm^{-1} and 1600 cm^{-1}. The vibrational modes confirmed the existence of spinel Cu doped $MgFe_2O_4$ structure for all samples [9,14,15,31].

3.4. Morphological study

3.4.1. SEM analysis

The surface morphology of the produced $Mg_{1-x}Cu_xFe_2O_4$ (X = 0.0, 25, 0.5, 0.75 and 1.0) nanoparticles were investigated using high resolution scanning electron microscopy, as illustrated in Fig. 7. Using ImageJ software, SEM micrographs' average particle size was calculated and shown in Table 3. Histograms of particle size distribution for S1, S2, S3, S4, and S5 from the SEM picture displayed in Fig. 7. SEM micrograph of $Mg_{1-x}Cu_xFe_2O_4$ samples show that all the samples have a close settlement of homogenous nanoparticles (with round shapes). In Fig. 7, S1 and S5 samples exhibits the existence of pure $MgFe_2O_4$ and $CuFe_2O_4$ nanoparticles, and Fig. 5 S2, S2, S3 provides pictures of Cu-doped Mg ferrite nanoparticles that are homogenous and agglomerated with diameters ranging from 59 $\pm$ 0.29 to 85 $\pm$ 0.23 nm. Copper ions (Cu^{2+}) have a lower ionic radius than iron ions (Fe^{2+}/Fe^{3+}), the main elements of $MgFe_2O_4$. When copper is replaced into the crystal lattice of $MgFe_2O_4$, the lattice structure may shrink. This contraction leads to a more compact arrangement of atoms and a smaller entire particle size. Copper ions can operate as nucleation sites or crystal growth inhibitors, resulting in the production of smaller nanoparticles for sample S2, S4, and S5. The addition of copper ions can alter phase transition behavior of $MgFe_2O_4$ nanoparticles. Copper doping may accelerate stabilize certain crystal phases associated with reduced particle sizes. Controlling the reaction conditions and dopant concentration can aid in the creation of finely distributed nanoparticles with smaller sizes [46]. Magnetic interactions between the particles as a result nanoparticles are agglomerated [14]There are particles of different sizes that are round and almost spherical in shape. S3 samples have the maximum particle size of 85 $\pm$ 0.23 nm because Cu doping may cause the generation secondary phases or crystal defects, which affect particle growth [46].

While S5 samples have the minimum particle size of 59 $\pm$ 0.29 nm. Pure magnesium ferrite nanoparticles are more spherical (nearly) in shape and uniformly dispersed than doped nanoparticles. The dopants have had a minor impact on the morphology of the sample. SEM images of S2 ($Mg_{0.75}Cu_{0.25}Fe_2O_4$), S3 ($Mg_{0.5}Cu_{0.5}Fe_2O_4$), and ($Mg_{0.25}Cu_{0.75}Fe_2O_4$) indicate that the produced particles are agglomerated due to the nanoparticles' strong magnetic interaction and high surface energy [10]. It also observed that increased the porosity of doped samples [52]. The spherical structure and particle aggregation shown in the SEM picture of doped nanoparticles may be the result of the sol-gel fabrication procedure.

3.4.2. TEM analysis

Cu-doped magnesium ferrite ($Mg_{0.5}Cu_{0.5}Fe_2O_4$) nanoparticles were used for carried out for Transmission electron microscopy
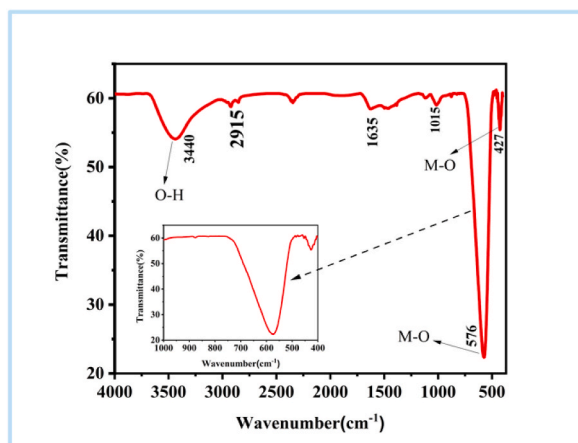

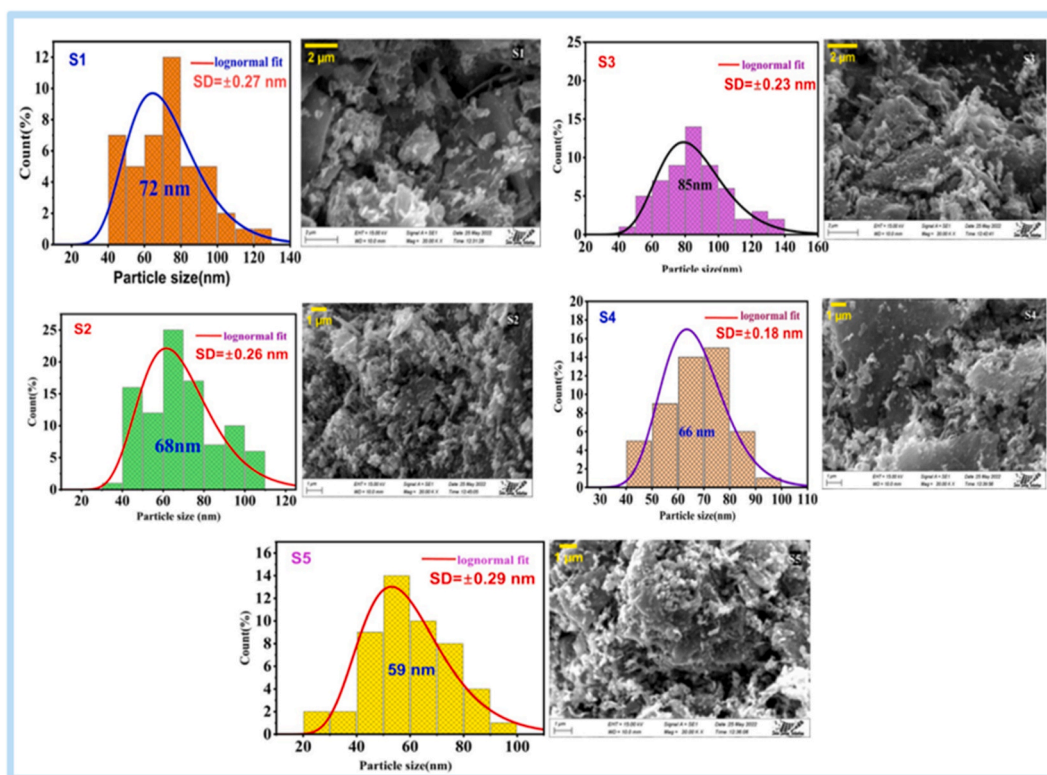**Fig. 6.** FTIR spectra of $Mg_{1-x}Cu_xFe_2O_4$ (x = 0.50) nano ferrite.

Fig. 7. SEM micrograph of $Mg_{1-x}Cu_xFe_2O_4$ (X = 0.0, 25, 0.5, 0.75 and 1.0) nanoparticles.

Table 3
Average particles size of $Mg_{1-x}Cu_xFe_2O_4$ nanoparticles.

Sample ID	Average Particle Size(nm)
S1	72 ± 0.27
S2	68 ± 0.26
S3	85 ± 0.23
S4	66 ± 0.18
S5	59 ± 0.29

(TEM) study. The data presented in Fig. 8(a–c) offer a comprehensive overview of TEM image of the $Mg_{0.5}Cu_{0.5}Fe_2O_4$ nanoparticles. We have selected $Mg_{0.5}Cu_{0.5}Fe_2O_4$ sample because it is the middle composition of the synthesized ferrites. Agglomerated nanoparticles of the sample seen in the TEM micrographs with a narrow size distribution as the nature of the nanoparticles to become agglomerated to reduce the Gibb's free energy [53].In Fig. 8(d) shown the histogram of the $Mg_{0.5}Cu_{0.5}Fe_2O_4$ nanoparticles. The histogram's estimated average particle size is 47.77 nm. It is noticed that the particle size distribution curve for x = 0.5 by normal SEM photographs exhibits an average particle size of 85 nm, while the particle size distribution for x = 0.5 (TEM images) exhibits 47 nm. TEM transmits an electron beam through an extremely thin sample, enabling high-resolution imaging of its interior structure. TEM generates images with a significantly higher magnification with better resolution than SEM. TEM can provide more precise particle size measurements since it allows for direct imaging of individual particles in three dimensions. By taking photos of particles in various orientations and utilizing image analysis algorithms and to obtained precise measurement of particle size. TEM also necessitates proper sampling, which includes the dispersion of the materials for electron transmission. While agglomeration can still happen, particularly in powders [21,54,55]. On the other hand, we used SEM not FE-SEM, So, the particle size obtained from TEM must be smaller than the size of the particles from SEM.

3.5. Compositional analysis

Energy dispersive X-ray (EDX) was used to investigate the compositional analysis of the samples of $Mg_{1-x}Cu_xFe_2O_4$ (x = 0.0, 25, 0.5, 0.75 and 1.0) nanoparticles to identify the elemental percentage in the sample and their atomic weight percentages. The results are given in Fig. 9 and Table 4. Samples S1 depicts the peaks of Fe, Mg, and O elements in pure Magnesium ferrite, while S2, S3, and S4 represents the peaks of Fe, Mg, Cu, and O elements in Cu doped magnesium ferrite and S5 shows the peaks of Fe, Cu, and O components
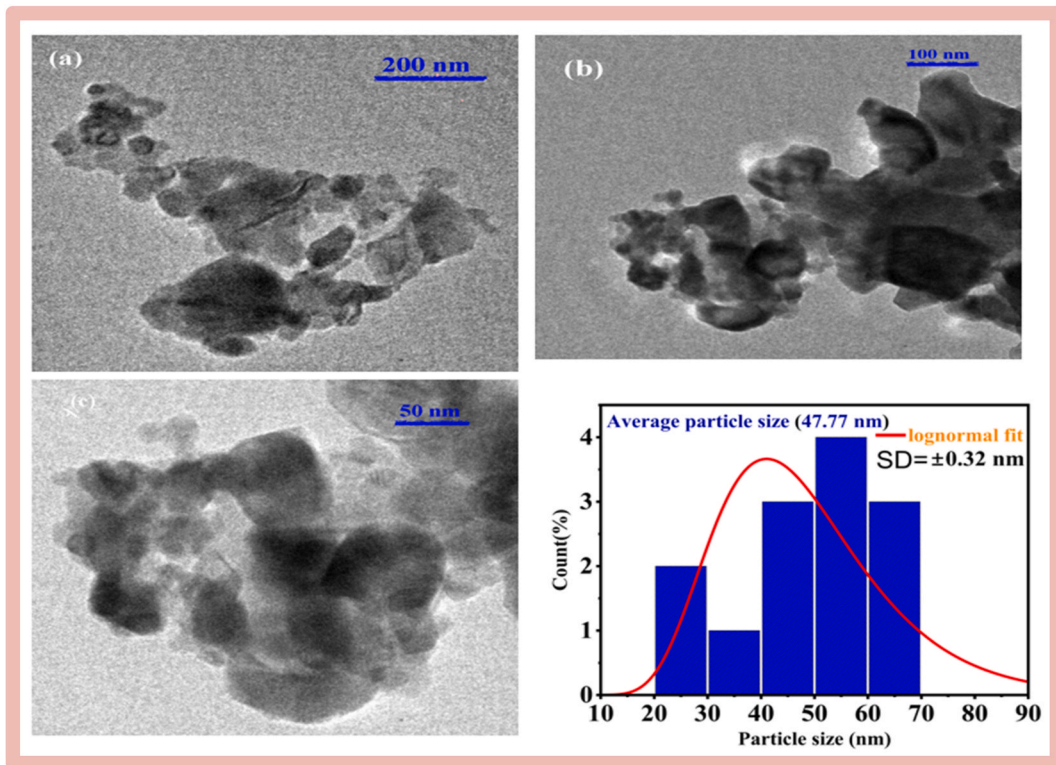
Fig. 8. (a), (b) and (c) TEM image of $Mg_{0.5}Cu_{0.5}Fe_2O_4$ nanoparticle of different magnification (d) particle size distribution.

in pure Copper ferrite. It has been shown that the atomic ratios of copper to iron and magnesium to iron are both quite near to the experimental ratio of 1:2 for S1 and S5 respectively. The expected percentage of Mg/Cu value corresponds well with the quantity of Mg/Cu employed in the Cu-doped Magnesium ferrite. The atomic percentage of Cu-doped magnesium ferrite are close to.
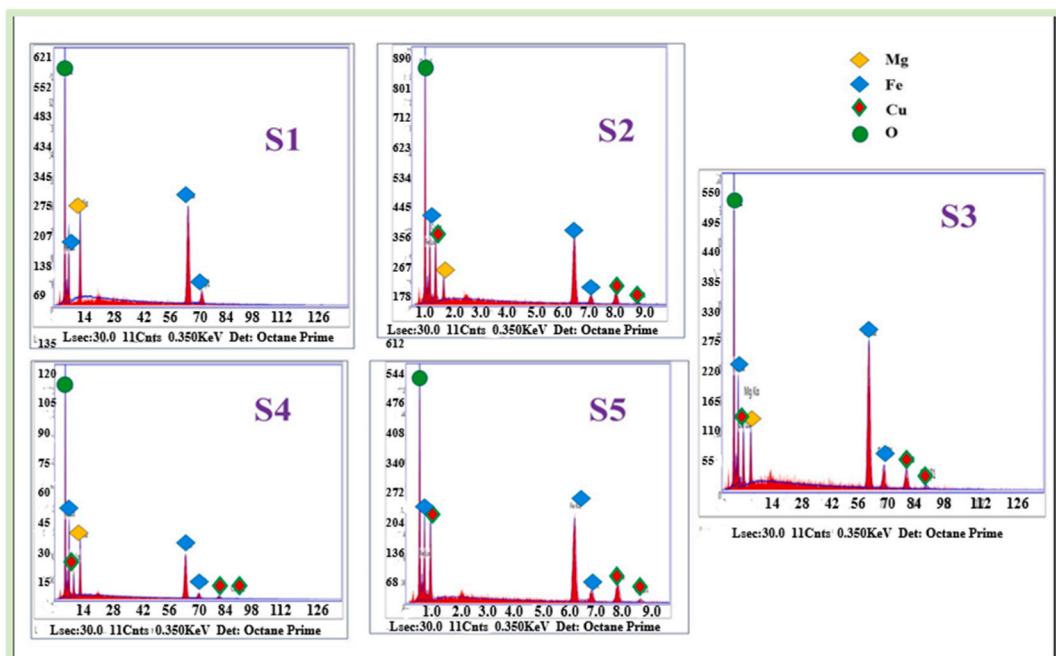

Fig. 9. Energy dispersive X-ray spectra of $Mg_{1-x}Cu_xFe_2O_4$ (X = 0.0, 25, 0.5, 0.75 and 1.0).

Table 4
EDX result of $Mg_{1-X}Cu_xFe_2O_4$ (x = 0.0, 25, 0.5, 0.75 and 1.0) nanoparticles.

| Sample Id	Atomic	Weight (%)		Ratio	Chemical formula
	Mg	Cu	Fe	Mg: Cu: Fe	
S1	13.73	0.00	42.15	0.65: 0: 2	$MgFe_2O_4$
S2	13.25	3.27	28.54	0.92: 0.23: 2	$Mg_{0.75}Cu_{0.25}Fe_2O_4$
S3	7.14	12.02	42.72	0.33: 0.56:2	$Mg_{0.50}Cu_{0.50}Fe_2O_4$
S4	4.62	12.31	33.68	0.27: 0.73: 2	$Mg_{0.25}Cu_{0.75}Fe_2O_4$
S5	0.00	17.38	38.46	0: 0.9:2	$CuFe_2O_4$

the theoretical value [3,18]. It is worth noting that the preparation conditions entirely promote the creation of combined ferrites and permit for the investigation of the influence of increasing Cu content on the characteristics of the Magnesium ferrite. The above outcomes support the synthesis of pure and Cu-doped $MgFe_2O_4$.

3.6. Magnetic properties

Fig. 10 illustrates a hysteresis plot showing the variation of magnetization (MS, emu/g) with respect to the applied magnetic field (H, Oe) for nanocrystalline $Mg_{1-X}Cu_xFe_2O_4$ samples, where (x = 0.0, 0.25, 0.5, 0.75 and 1.0). The saturation magnetization (M_S), coercivity (H_C), retentivity (Mr), net magnetization(μ_B), and magnetic anisotropy (K) are all tabulated in Table 5. Magnetic moments in nanoscale materials are influenced by various factors, including grain disorders, canted surface spins, oxygen deficiency, unsaturated chemical bonds, grain boundaries (GBs), GBs pinning, redistributions of metal cations, degree of inversion due to cation inversion factor, increased specific surface area and the formation of hematite ($\alpha - Fe_2O_3$) on the NPs surface [56–58].Unsaturated chemical bonds, low coordination numbers, anisotropic layers, and loss of long-range ordering on the surface of NPs create a disordered spin structure, resulting in a spin glass-like structure. Spin disorder, also known as canted surface magnetic spins, creates a spin-glass-like structure on NP surfaces, resulting in weak A-B exchange contacts and reduced M_S [56,57]. According to the study, the spinel ferrite behavior of synthesized nanoparticles is represented by the presence of coercivity and retentivity magnetization. The magnetic hysteresis curves clearly reveal that $MgFe_2O_4$ is a soft magnetic material, and when Mg^{2+} in $MgFe_2O_4$ is substituted by Cu^{2+} ions, the magnetic characteristics such as saturation magnetization (M_S), remanent magnetization (M_r), and coercivity (H_c) change dramatically, as shown in Fig. 10 [5,18,37].The M_S of the $Mg_{1-x}Cu_xFe_2O_4$ nanoparticles are seen to progressively increase as the Cu^{2+} concentration increases up to x = 0.5 and rapidly drop at x more than 0.5 (i.e., x = 0.75) (as shown in Table 5) [18,59]. The size, phase, and cation distribution, among other elements, have a significant impact on the Ms of spinel ferrite [1]. Because Mg^{2+} is non-magnetic and Cu^{2+} is paramagnetic, the Ms of $Mg_{1-x}Cu_xFe_2O_4$ nanoparticles is ascertained by the distribution of Fe^{3+} ions across tetrahedral and octahedral lattice locations. The samples $MgFe_2O_4$ and $CuFe_2O_4$ exhibited soft ferromagnetic activity, but $Mg_{0.75}Cu_{0.25}Fe_2O_4$ and $Mg_{0.5}Cu_{0.5}Fe_2O_4$, which had lower Cu^{2+} concentrations (x = 0.25, 0.5), demonstrated an increase in the ferromagnetic behavior. This suggested that Mg^{2+} ions filled the tetrahedral sites and Fe^{3+} ions inhabited the octahedral sites, whilst the dopant Cu^{2+} ions occupied either the octahedral or tetrahedral sites, resulting in excellent ferromagnetic characteristics [18,59,60]. Ms attained a maximum value of 28.96 emu/g when x = 0.5. The Ms value of the samples $Mg_{0.25}Cu_{0.75}Fe_2O_4$ and $CuFe_2O_4$ decreases as the concentration of Cu^{2+} in $MgFe_2O_4$ nanocrystals increases (i.e., 25.61 and 22.38 emu/g, respectively). Because dopant Cu^{2+} ions preferentially hold the octahedral sites, they may push Fe^{3+} to the A-sites, lowering the value of M_S.

The migration towards A-sites, however, would result in an increase in the concentration of Fe^{3+} in A-sites, which leads to anti-parallel spin coupling and spin canting, weakening the A-B exchange coupling and lowering the net magnetic moment [18]. Magnetic
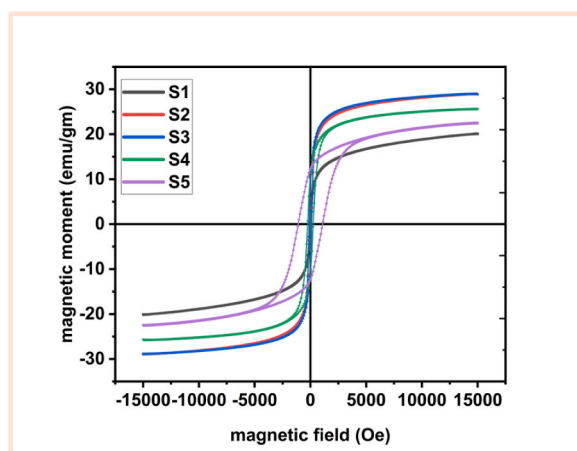
Fig. 10. M–H curve of $Mg_{1-X}Cu_xFe_2O_4$(X = 0.0, 0.25, 0.5, 0.75 and 1.0) NPs.

Table: 5
The values of coercivity (Hc), net magnetization (μB), saturation magnetization (Ms), retentivity (Mr), magnetic anisotropy (K), and rectangular ratio (Rs) of Mg$_{1-x}$Cu$_x$Fe$_2$O$_4$.

Sample	Saturation magnetization Ms (emu/gm)	Retentivity Mr (emu/g)	Coercivity Hc (Oe)	Magnetic anisotropy K × 103 (ergcm-3)	μB	Rectangular ratio RS (Mr/Ms)
MgFe$_2$O$_4$	20.12	2.32	54	1.13	0.720	0.115
Mg$_{0.75}$Cu$_{0.25}$Fe$_2$O$_4$	28.92	7.43	93	2.80	1.086	0.256
Mg$_{0.5}$Cu$_{0.5}$Fe$_2$O$_4$	28.96	8.45	103	3.10	1.138	0.291
Mg$_{0.25}$Cu$_{0.75}$Fe$_2$O$_4$	25.61	10.81	244	6.50	1.053	0.422
CuFe$_2$O$_4$	22.38	12.39	1102	25.69	0.958	0.553

characteristics are also significantly influenced by the kind and concentration of cation substitution. In Eq. (14) The magnetic moment per atomic unit is represented as according to the Neels two sublattice model of ferrimagnetism,

$$M(X) = \left| M_{B(X)} - M_{A(X)} \right| \tag{14}$$

Where, M$_B$ and M$_A$ respectively represent the magnetic moments of the B- and A-sublattice in μB.

The M$_S$ value is based on net magnetic moment. According to the literature, copper ferrite and magnesium ferrite have an inverted spinel structure, with the octahedral positions being preferred by the Mg^{2+} and Cu^{2+}cations. Both Mg^{2+} and Cu^{2+} are divalent ions, however Cu^{2+} is magnetic whereas Mg^{2+} is not. The cationic distribution on tetrahedral and octahedral lattice sites has a significant effect on the magnetic susceptibility (M$_S$) of spinel ferrite nanoparticles. Fe^{3+} likes to occupy both A-sites and B-sites in Cu-doped Mg ferrite, whereas Mg^{2+} and Cu^{2+} ions prefer to reside in the respective A- and B-sites. Surface effects alter the magnetic properties of NPs through exchange interactions at A and B sites of the crystal structure [56,57]. M$_S$ is reduced when the Cu concentration is greater than 0.5 due to the A-B exchange interaction, which is weaker than the B–B interaction. M$_S$ attained its maximum (28.96 emu/g) when x is 0.5, which corresponded to prior findings [18,37].

The approximated M$_S$ and μ$_B$ values are listed in Table 5 using Eq. (15),

$$\mu_B = \frac{MW \times M_S}{5585} \tag{15}$$
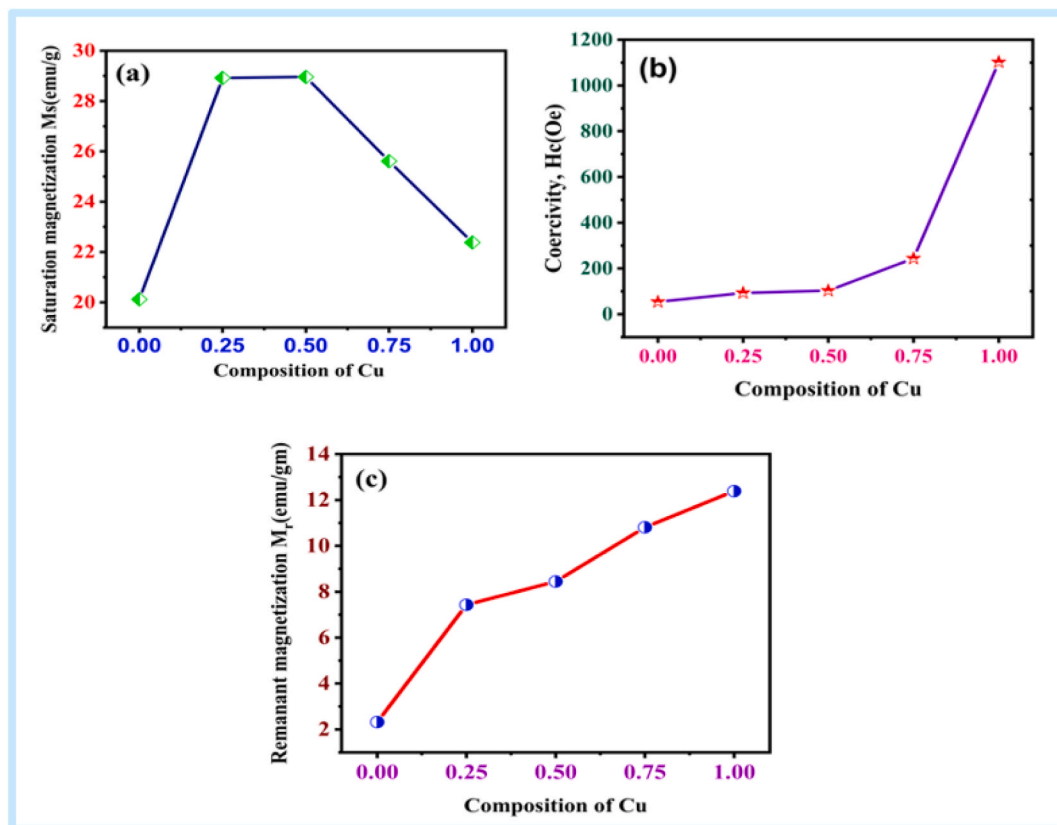
Fig. 11. Change of (a) saturation magnetization, (b) coercivity (Hc), and (c)saturation magnetization (Ms) Mg$_{1-x}$Cu$_x$Fe$_2$O$_4$ with Cu content.

In Eq. (15) Where MW is the molecular weight of the powder sample and M_S is the saturation magnetization of the powder sample. The μ_B values at first increase for x = 0.25 and 0.5 and decrease for x = 0.75 in the magnesium ferrite nanoparticles [1,5]. In Fig. 11(a-c) depicts a comprehensive overview of the Change of (a) saturation magnetization, (b) coercivity (Hc), and (c)saturation magnetization (Ms) $Mg_{1-x}Cu_xFe_2O_4$ with Cu content.

Coercivity and remanent magnetization increased when dopants' content was increased [17]. The increase in magnetic anisotropy of ferrite nanoparticles, which prevents the magnetic moment resulting from alignment in an applied field, is responsible for the increase in saturation magnetization and coercivity [61]. This sort of behavior is related to the size dependency of H_C in the magnetic multi-domain region. The nanoparticles in this range have several magnetic domains, allowing for easy domain wall motion and magnetization reversal. This reduces H_C values by lowering domain wall energy. Equation (16) is used to determine the magnetic
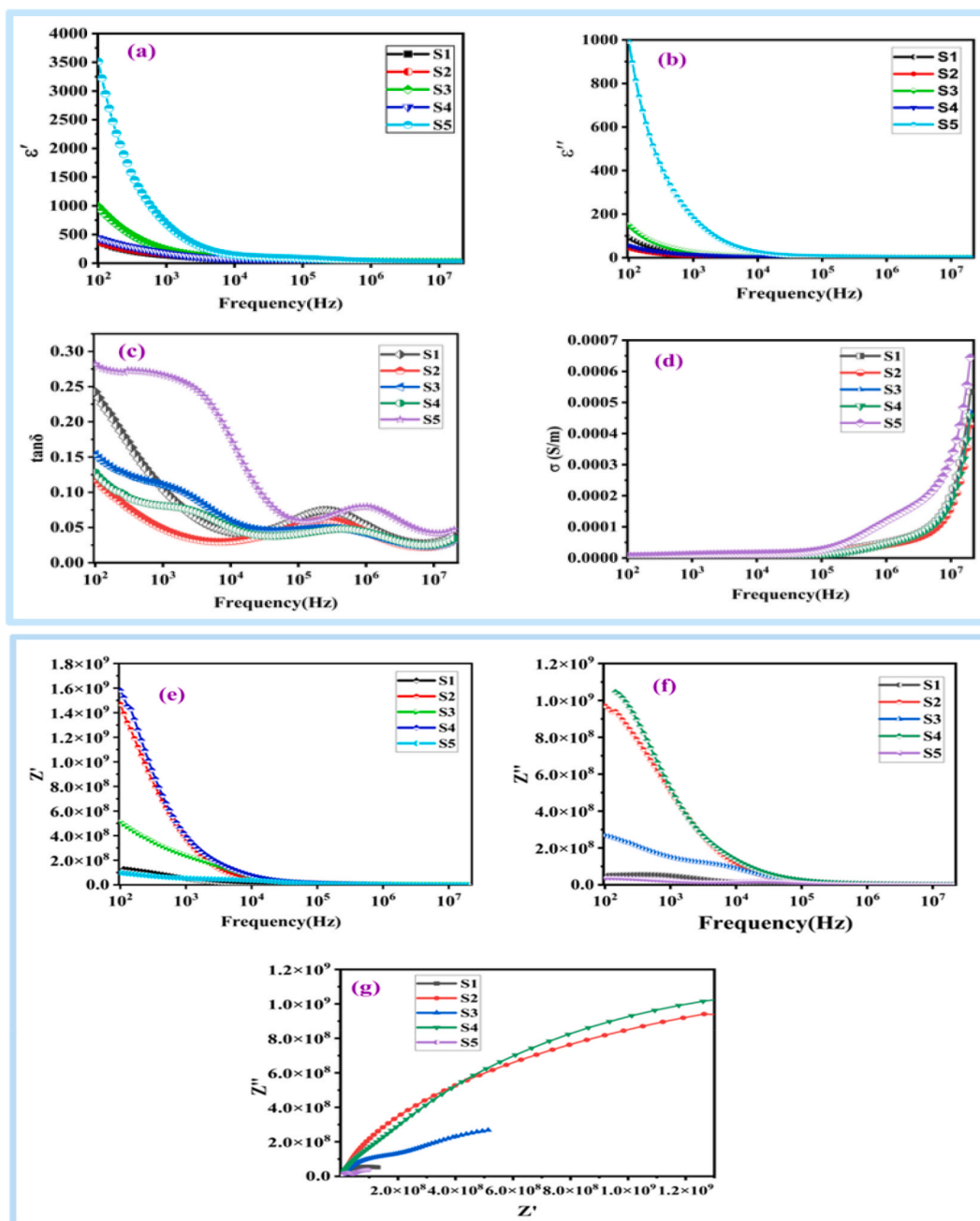
Fig. 12. Variation of (a) real dielectric constants (ε') (b) imaginary dielectric constants (ε'') (c)loss tangent (tanδ) (d) ac conductivity versus frequency (f in Hz) (e) real impedance (Z') (f) imaginary impedance (Z'') and (g) Cole-Cole curves of impedance of the $Mg_{1-x}Cu_xFe_2O_4$ nanoparticles.

anisotropy (K) values, which are displayed in Table 5 as numbers [51]

$$K = \frac{M_S \times H_C}{0.96} \qquad (16)$$

Magnetic anisotropy is affected by nanoparticle crystallinity, surface area to volume ratio, and changes in interparticle interaction [15,60,62].The high coercivity value is mostly attributable to the anisotropy of Cupper ions at the octahedral (b) site due to the strong spin-orbit coupling [63]. Higher H_C owing to spin disorder at the particle surface, canted spins, and spin-glass-like structure at the surface layers caused by chemical disorder and broken bonds.

The rectangle ratio computed from equation (17) is a measurement of how easily the side of magnetization reorients once the magnetic field is removed to the easiest axis.

$$R_S = \frac{M_r}{M_s} \qquad (17)$$

The rectangular ratio is found to be between 0.115 and 0.553. The values of S1 (0.115), S2 (0.256), S3 (0.291), S4 (0.422) and S5 (0.553) demonstrate that the ferrites are soft magnets with single domain nanoparticle properties. Because the Rs value is smaller than 0.5, the particles interact via magnetostatics. Magnetostatic interactions are responsible for the aggregation of $MgFe_2O_4$ and Cu-doped magnesium ferrite nanoparticles, as seen in the SEM picture (Fig. 7.) [15,62].

3.7. Analysis of electrical properties

3.7.1. Study of permittivity and ac conductivities

The dielectric parameters of the samples are studied at frequencies ranging from 100 Hz to 2×10^7 Hz. The real(ε') and imaginary (ε'') components of permittivity, loss tangent (tanδ), and AC conductivity(σ_{AC}) are calculated using Eq. 18–20, the formulae below.

$$\varepsilon' = \frac{Cpd}{\varepsilon_0} \qquad (18)$$

$$\tan\delta = \frac{\varepsilon''}{\varepsilon'} \qquad (19)$$

$$\text{And } \sigma_{AC} = 2\pi f \varepsilon_0 \varepsilon' \tan(\delta) \qquad (20)$$

In these equations, Cp seems to be the capacitance of the spinel ferrite tablet placed among two circular electrodes with surface area of A, the thickness of the tablet is d, and the vacuum permittivity ε_0 is $(8.85 \times 10{-}12 F/m)$ [26,50].

Dielectric parameters are particularly valuable tools for understanding the frequency dependent conduction process in ferrite. The dielectric properties provide us with useful information about the ability of dielectric materials to store electric charges. Fig. 12 (a) and (b) demonstrate the real part's and the imaginary part's respective relative permittivity against frequency. Permittivity lowers with rising frequency and remains relatively constant at higher frequencies, according to the graph. The Koop's model helps explain this tendency. In this concept, ferrite materials are assumed to have conducted ferrite grains separated by a tiny grain border coating having minimal conductivity. As frequency increases, the values of ε'' and tan(δ) drop due to shorter relaxation times of electrical or interfacial dipoles [47,54,55]. Lower frequencies show higher values of ε'' and tan(δ), indicating the presence of interfacial (space--charge) polarization caused by charge carriers trapped at grain boundaries. When an electric field is applied to this arrangement, charge carriers collect at the borders. This event causes polarization of space charge [1,36]. Charges are distributed to the grain borders because of the hopping mechanism between the ferric ions as well as the octahedral sites:

$Fe^{2+} + Fe^{3+} \longleftrightarrow Fe^{3+} + Fe^{2+}$ [
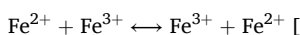
It should be mentioned that electron hopping between iron and the other ions ($Mg^{2+} + Fe^{3+} \longleftrightarrow Mg^{3+} + Fe^{2+}$) is extremely improbable to occur since it causes an alteration in the initial and final ionic states of ferrite's [64–66]. Because of the insulating nature of the grains' borders, electrons are accumulated there. As a result, permittivity and polarization are particularly high having related to low frequency range. However, polarization decreases with increasing frequency because transmission between Fe^{2+} and Fe^{3+} cations does not suit the frequency of the electromagnetic wave. As a result, permittivity diminishes at high frequencies and approaches a basically constant value [1,26,52,67].

Furthermore, non-monotonous changes in dielectric constant values with crystallite size may be observed. These dielectric constant values can be linked to structural changes produced by Cu entry into the system. Cu^{2+} ions can occupy both tetrahedral A-sites and Octahedral B-sites, impacting competition between Fe^{3+} and Mg^{2+} ions for tetrahedral and octahedral positions in an inverted spinel. Thus, as Cu^{2+} ions rise at A-sites, some Fe ions from B-sites move to the A-sites. The outcome is, the number of Fe^{2+} and Fe^{3+} ions at ferrites' B-sites, which are essential for electrical transmission, would reduce. The dielectric constant of Cu substituted Mg ferrite has been changed by cation displacement between A and B sites [64]. According to theory, surface polarization in ferrites is primarily caused by.

Space charge polarization, conductivity, and charge hopping between two localized states. As a result, the nonlinear fluctuation in dielectric constant might be caused by the insertion of Cu^{2+} ions, which lowers the quantity of Fe^{3+} ions on B-sites, which is responsible

for both space charge polarization and hopping interchange between two localized states. It is worth noting that the highest dielectric constant dispersion was observed for x = 1.0 and 0.75 at 4.5 MHz in Table 6 copper concentration, most likely due to the production of the presence of Fe^{2+} ions on octahedral sites and results in a low resistive grain boundary phase [31,50].

Fig. 12 (c) illustrates the fluctuation of dielectric loss tangent with frequency as compute at ambient temperature and estimated by Eq. (19). Table 6 at 4.5 MHz frequency indicates the dielectric loss. We can observe that as frequency increases, the dielectric loss tangent tan(δ) decreases. Dielectric loss values were found to be very low at higher frequencies because domain wall motion is hindered. Tan(δ) changes with frequency in the same way as permittivity changes. This is owing to the close relationship between ferrite dielectric efficiency and the conduction process. The maximum overall dielectric loss is shown for the highest doped sample when evaluating the overall variance of dielectric loss for each sample, which exhibits monotonous approach with dopant concentration [59].The hopping of the electron cannot keep up with the fluctuation in the electric field of the high-frequency section of an electromagnetic wave [26].

The AC conductivity of the samples is depicted in Fig. 12 (d). The AC conductivity changes with frequency are divided into two parts: for one with a lower frequency (500–2000 Hz) and above that for one with a high frequency (2000 to 10^7 Hz). The conductivity slowly goes up at low frequencies and rapidly at high frequencies as the frequency increases. The low frequency region's activity is linked to the weak electron hopping or low hopping possibility in this region [68,69]. The polaron type of conduction mechanism in ferrites causes a linear rise in AC conductivity with frequency [70]. There are two sorts of polarons: tiny and giant. The tiny polaron model increased AC conductivity as frequency increased, while the big polaron model decreased it. According to Alder and Feinleib [55], the tiny polaron model is responsible for direct frequency-dependent conduction. The mixed (small/large) polaron type of conduction mechanism causes a minor reduction in AC conductivity at specific frequencies [54,70]. In higher frequencies, however, it is discovered that the AC conductivity may be calculated using Eq. (21) below.

$$\sigma_{AC}(\omega, T) = A(T)\omega^n \tag{21}$$

the angular frequency (ω) is a parameter that's depends on A(T) temperature, is of applied field and n is a power-law exponent such that $0 \leq n \leq 1$. A value of n between 0.8 and 1 has been recorded for certain spinel ferrite. As a result, the rather steep rise in conductivity for specific frequencies may be justified by this equation, as seen in Fig. 12 (d). The rise in ac conductivity of ferrites with frequency is characterized by the frequency dependent ac conductivity characteristics are described using the Maxwell-Wanger two-layer model and Koop's phenomenological approach [71]. Ferrites materials contain high conducting grains isolated by resistive grain boundaries. Depending on electron hopping and space charge polarization, the grains are extremely conductive at high frequencies but display poor conductivity at low frequencies. As the frequency of the applied field rises, the grains become more active by raising the hopping frequency between ions. Furthermore, the pumping pressures of the applied frequency assist charge carriers in transferring between distinct localized states and releasing trapped charges from additional trapping locations. The electrons and charge carriers contribute to the valence-induced conduction process caused by valence swap between the cations contained inside the sublattices. As a result, all the compositions exhibit a significant increase in ac conductivities [72]. However, the dielectric behavior of the conduction mechanism is.

significantly interrelated with these hopping charge carriers. Because polarization was unable to follow ac field alterations as the applied field frequency grew, the dielectric constant decreased and became constant. As a result, the overall polarization decreases, and the conductivities increase for all ferrite samples. However, in the low frequency zone, the alternating current field does not supply enough energy to the carriers to overcome these insulting obstacles. The samples act like semiconductors, with a flat plateau. Because of the examined ferrites' microstructural characteristics and band gaps, conductions dispersed at a high frequency zone. Furthermore, oxygen shortage is critical to charge carrier movement. The density of oxygen vacancies increases conductivity. The variation in particle size with composition, alters the number of grain borders, which affects electron mobility from one grain to the next. The sample oxygen vacancy content may impact due to the grain boundary's conductive properties. As an outcome, electron hopping is critical in enhancing the conductivity of the investigated ferrite [1,51].

Impedance spectra study: Fig. 12(e) depicts the frequency reliant real part of impedance (Z') doped $MgFe_2O_4$ nanoparticles. The observed decrease in real component of impedance of this ferrite sample as frequency increases supports the observed rise in ac conductivity as frequency increases. The rise in frequency causes a reduction in the real part of impedance (Z') because of space charge polarization in Cu doped $MgFe_2O_4$ spinel ferrite nanoparticles. Fig. 12(f) illustrated the frequency dependence imaginary part of impedance (Z'') for the prepared nanoparticles. The imaginary portion of impedance decreases as frequency increases. This doped nanoparticles' drop in imaginary part of impedance is correlated with its inverse relationship with frequency [71–74]. Koop's theory assumes conductive grains and nonconductive grain borders. Grain boundaries are often considered flaws in the lattice. The Cole-Cole plot is a popular method for determining how grains and grain boundaries affect the overall electrical conductivity of a dielectric nanomaterial [70]. To analyze the ambiguity caused by the existence of grain boundary impact at ambient temperature, the imaginary

Table 6
Electrical (@4.5 MHz) parameters of $Mg_{1-x}Cu_xFe_2O_4$.

Parameter	X = 0.00	X = 0.25	X = 0.50	X = 0.75	X = 1.00
Dielectric constant	13.63	13.72	14.91	13.91	15.61
Dielectric loss	0.389	0.3163	0.375	0.376	0.805
AC conductivity(S/m)	9.89×10^{-5}	7.96×10^{-5}	9.50×10^{-5}	9.51×10^{-5}	9.50×10^{-4}
tanδ	0.0286	0.0230	0.0252	0.0270	0.0514

part of impedance (Z″) was plotted against the real part of impedance(Z′), as shown in Fig. 12(g) [53]. This finding clearly indicates the appearance of dipolar and space polarization in the analyzed material, with peaks appearing because of dipolar contribution [20,75]. The Nyquist plot of the showers in Fig. 12 (e) and (f) shows a similar form but significantly different particle sizes. Metallic coating can result in the creation of a single or several semicircles in the high frequency zone, followed by a low frequency region. The semicircle in the high frequency zone reflects the coating response, while the loop in the low frequency region depicts the physicochemical phenomena at the metal/coating/solution interface [54]. At all doped concentrations, the Nyquist figure confirms the presence of just one semicircular arc. The impedance response from the grain and the grain structure are discovered to intersect, and the overlap is substantial if the time constant of distinct strategies vary by less than a factor of 100. The arc's semicircular radius arc shown to rise as the amount of doping increases. It is worth noting that the radius of the impedance arc initially reduces and then increases, indicating that the material has a critical composition [14,25].

3.8. Optical properties

The most essential characteristics of nanoparticles are optical absorbance and band gap energy. It is commonly known that the band gap is still the same in certain compositions with identical ingredients, however the band gap energy fluctuates depending on the percentage of element in the composition [76,77].The investigation of optical reflection spectra is an excellent method for analyzing the band gap and nanocrystalline materials' band energy. At room temperature the optical absorbance of nanocrystalline $Mg_{1-x}Cu_x$-Fe_2O_4 ferrite was measured in the wavelength range 380–780 nm. In Fig. 13 was displayed (a) UV–visible diffuse reflectance spectra vs wavelength and (b), (c), (d), (e), (f) direct band gap energy $Mg_{1-x}Cu_xFe_2O_4$ nanoparticles. Magnesium ferrite spinel exhibits strong optical absorption bands of about 300–400 nm Fig. 13(a). These bands are attributed to Fe^{3+} ions in octahedral coordination [78]. D. Shahid et al. estimated band gap energy for $MgFe_2O_4$ is 2.0–2.2 eV. The Kubelka- Munk Function may estimate the optical absorption coefficient(α) via optical reflectance data using Eq. (22) below

$$F(R) = \frac{(1-R)^2}{2R} \tag{22}$$

Where, R is the diffuse reflectance. The basic absorption, which corresponds to the value of the optical bandgap of the produced nanomaterials may be determined by excitation of electrons from the valence band to the conduction band [9,67,72].The optical direct band gap energy (Eg) is measured by drawing a graph (Fig. 13b-f) between $[F(R)h\nu]^2$ and $h\nu$ this is generally known as Tauc's relation [79]. The calculated values of direct band gaps of $Mg_{1-x}Cu_xFe_2O_4$ (x = 0.0, 0.25,0.5, 0.75 and 1.00) nanoparticles are 1.77, 1.78, 1.90, 1.96 and 2.00 eV, respectively (Fig. 13, Table 7). In Fig. 13(a), the F(R) spectra of Cu-doped $MgFe_2O_4$ NPs around 480 nm show a shift in the band edge toward higher wavelengths (λ) when Cu concentration increases, resulting in a smaller band gap. Many-body phenomena may impact Eg gap of produced nanoparticles. The optical band gap (Eg) is mainly affected by nanoparticle shape and size, particle dispersion, lattice strain, and dislocation density. As prepared NPs generate gaps due to energy levels above and below the VB and CB, resulting in lower band gaps. The drop in Eg might be attributed to the entrance of dopant Cu^{2+} ions into the $MgFe_2O_4$ lattice, replacing Mg^{2+} sites with Cu^{2+} ions. Replacing Mg^{2+} sites in the $MgFe_2O_4$ lattice with Cu ions creates impurity levels between the VB and CB, while including Cu^{2+} creates vacancies in the band gap, reducing optical band gaps (Eg) [46,78,80,81]. There is no consistent change in Eg in as-prepared NPs. For the specimen x = 0.25 Eg is decrease 1.78 eV. Diminution in Eg might be linked to the change from VB to impurity levels in the forbidden band gap, rather than the excitonic transition itself. Creating (O^{2-}) empty space between the VB and CB reduces Eg gaps considerably. The reduction in Eg of $Mg_{1-x}Cu_xFe_2O_4$ NPs is caused by many-body effects on the VB and CB, resulting in lower optical band gaps due to electronic interaction and Cu impurities.

For the other samples (except x = 0.25), particle size reduces progressively with increasing Cu^{2+}ions, as revealed by SEM analysis, resulting in greater optical band gaps.

Smaller particles have fewer atoms, leading to less overlapping molecular orbitals and a broader optical band gap. This widens the space between the HOMO and LUMO orbitals, resulting in a broader band gap. HOMO is a nucleophilic characteristic that donates electrons from the shallowest orbital, whereas LUMO is an electrophilic characteristic that accepts electrons and represents electron enthalpy [46,56,78,81,82].

The indirect band gap energy is calculated by plotting a graph between $[F(R)h\nu]^{1/2}$ and $h\nu$ (Fig. 14a-e) for the sample of S1, S2, S3, S4, and S5 respectively. The band gap of $Mg_{1-x}Cu_xFe_2O_4$ nanoparticles is determined to be (x = 1.78, 1.61, 1.91, 1.86 and 1.98 eV, respectively [83]. Our findings are like those reported for Cu-doped magnesium ferrite nanocrystals. It is noticeable that the band gap of the Cu-contain magnesium ferrite samples is larger than that of pure $MgFe_2O_4$. The band gap energy increases for Cu-containing nanoparticles with x = 0.5, 0.75 and 1.0 then decreases for x = 0.25. Copper doping affects magnesium ferrite's bandgap, affecting its optical characteristics. Changing the copper content can move the bandgap, affecting light absorption and emission. A 0.25 Cu-doped sample has a different bandgap than other samples, which affects its optical performance. Specific copper concentrations in nanoparticles or thin films cause surface plasmon resonance (SPR) [55,84]. The rise in band gap can be due to an increase in lattice constant as Cu content increases [72]. The change in Eg is equivalent to the change in the lattice parameter. When the proportions of the lattice are lowered, electrons expand more closely coupled to atoms, demanding a high excitation energy [50,75,85]. Band gap values are well reported to be controlled by film thickness, crystallite size, lattice constant, purity, stoichiometry, charge carrier concentration, and lattice strain [9,76].

It is worth noting that the magnitude of the direct and indirect band gaps for x = 0.25 drop, might be owing to the quantum size effect occurring in a semiconducting thin layer. Furthermore, this may be supported by the fact that the new defect may be introduced
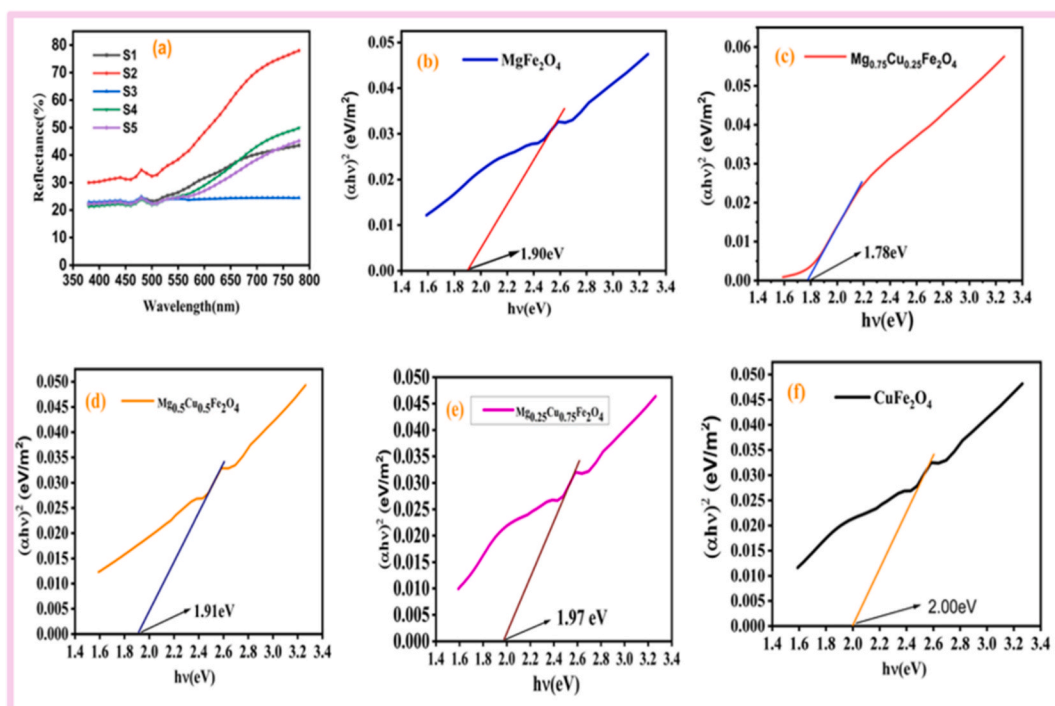
Fig. 13. (a) UV–visible diffuse reflectance spectra vs wavelength and (b), (c), (d), (e), (f) direct band gap energy $Mg_{1-x}Cu_xFe_2O_4$ nanoparticles.

Table 7
Band gap energy values for the investigated samples.

Samples	Band gap(eV)	
	Direct	Indirect
S1	1.77	1.78
S2	1.78	1.61
S3	1.90	1.91
S4	1.96	1.86
S5	2.00	1.98

following Cu^{2+} substitution. Additionally, Cu^{2+} dopant contributes more electrons due to Cu^{2+} lower electron affinity contrasted to Fe^{3+}, which occupies the energy levels near the base of the conduction band. All the produced nanoparticles exhibit significant reflectance in the wavelength range investigated, emphasizing their potential use in optical systems and visible light photocatalysis [76,86,87].

4. Conclusions

$Mg_{1-x}Cu_xFe_2O_4$ (x = 0.0, 0.25, 0.5, 0.75 and 1.00) nanoparticles were successfully prepared employing the very simple and cost-effective sol-gel technique using citric acid as the chelating agent. XRD patterns of the materials proved the development of the cubic spinel phase structure supported by two identical vibrational bands at 576 cm^{-1} and 427 cm^{-1} for stretching vibrations of metal-oxide tetrahedral and octahedral sites. The x-ray peak profiling was carried out through Debye-Scherrer, Halder-Wagner and Size strain plot method to determine the crystallite size (10.81–22.87 nm) and dislocation density. The lattice parameter of Cu-doped $MgFe_2O_4$ reduced from 8.4005 to 8.2873 Å with increasing the Cu concentration. The SEM and TEM images indicate the agglomeration of particles, and the average particle size of the materials are 59–85 nm in range and in case of S3, 85 nm from SEM where 47 nm from TEM. The EDS spectra confirms the purity of the nanomaterials very close to the theoretical stoichiometric ratio. The UV–Vis–NIR spectroscopy reveals that the band gap energy of the synthesized ferrites was in the range 1.71–2.04 eV which is suitable for photocatalyst. In the current investigation, Coercivity and retentivity enhanced as Cu-content increased and maximum for pure $CuFe_2O_4$ 1102 Oe and 12.39 emu/gm, respectively. The soft ferromagnetic property of Cu^{2+} ions increase (up to x = 0.5), changing the form of M − H loops. Magnetization at the highest field increases monotonically with rising Cu content to x = 0.5 and decreases towards x = 1.0, which is due to changes in the cationic distribution at tetrahedral and octahedral sites. Smaller coercivity results showed the soft magnetic nature of these pure and Cu doped $MgFe_2O_4$ and larger value of coercivity in $CuFe_2O_4$ showed the hard in magnetic nature.
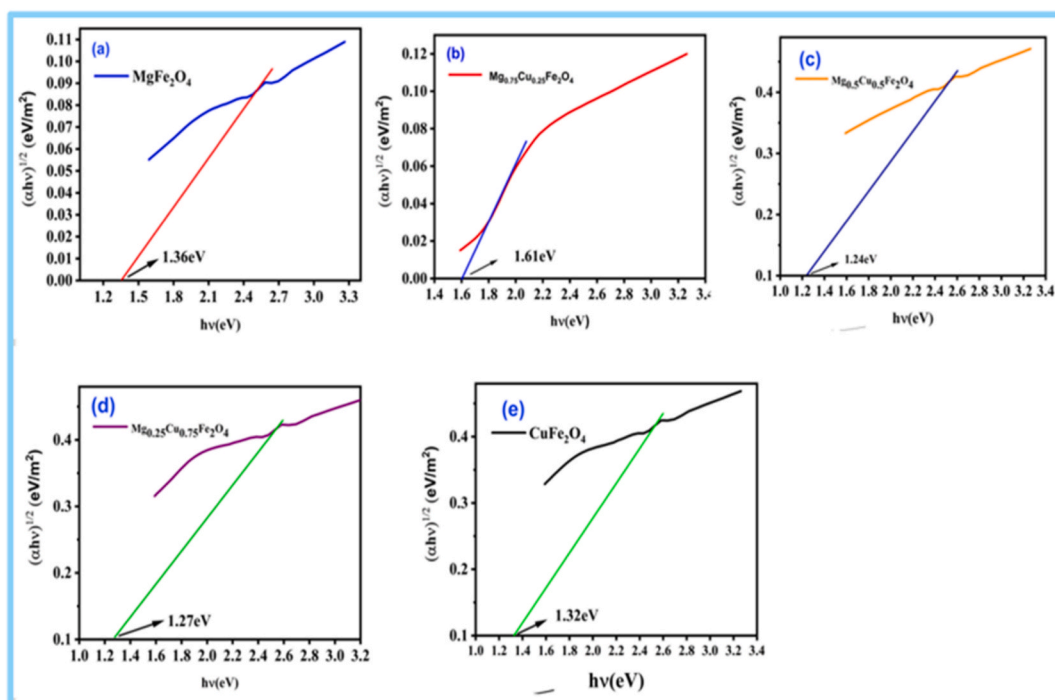
Fig. 14. (a–e) Indirect band gap plots of $Mg_{1-x}Cu_xFe_2O_4$ nanoparticles.

Substituting Cu^{2+} ions for the Mg^{2+} ion affects the magnetic characteristics of the studied materials. The room temperature magnetization and coercivity values clearly indicate the changes with Cu doping. These values make the sample suitable for recording media at room temperature. As a result, the distinct changes in the characteristics of Cu-doped magnesium ferrite nanoparticles can be attributed to divalent metal cation rearrangements at different lattice locations. In doped samples, increasing the Cu concentration at (x = 0.75 and 1.00) led to the best results for the dielectric constant, dielectric losses, and alternating current conduction. The impedance was raised to a specified doping level. Copper-doped magnesium ferrite may have potential use in microwave frequency devices based on the positive electrical characteristics results. The synthesized nano Mg–Cu nanoparticles will be applied as humidity sensor, gas sensor, microwave devices and photocatalyst.

CRediT authorship contribution statement

Sushen Chandra Devsharma: Writing – original draft, Visualization, Software, Investigation, Formal analysis, Data curation. **Md Lutfor Rahman:** Writing – review & editing, Visualization, Supervision, Resources, Project administration, Methodology, Investigation, Funding acquisition, Data curation, Conceptualization. **Md Jakir Hossain:** Writing – review & editing, Visualization, Validation. **Bristy Biswas:** Visualization, Validation, Data curation. **Md Farid Ahmed:** Visualization, Validation, Data curation. **Nahid Sharmin:** Writing – review & editing, Resources, Project administration, Funding acquisition.

Declaration of competing interest

The authors declare that they have no known competing financial interests or personal relationships that could have appeared to influence the work reported in this paper.

Acknowledgements

References

[1] N. Jahan, M.N.I. Khan, M.R. Hasan, M.S. Bashar, A. Islam, M.K. Alam, M.A. Hakim, J.I. Khandaker, Correlation among the structural, electric and magnetic properties of Al3+ substituted Ni-Zn-Co ferrites, RSC Adv. 12 (24) (2022) 15167–15179, https://doi.org/10.1039/d1ra09354a.

[2] A. Poddar, S. Halder, S.I. Liba, S.M. Hoque, S.S. Sikder, Study of the effect of quenching on microstructural and magnetic properties of Cu-doped Mg-ferrite, Adv. Condens. Matter Phys. 2022 (2022), https://doi.org/10.1155/2022/3354087.

[3] A.A. Khan, S.N. Khan, A. Mir, Structural and electromagnetic characterization of yttrium doped copper ferrite, J. Magn. Magn Mater. 559 (2022), https://doi.org/10.1016/j.jmmm.2022.169510.

[4] R. Kant, J. Jhabarmal, A.K. Mann, A review of doped magnesium ferrite nanoparticles: introduction, synthesis techniques and applications. *2018 IJSRSET* 4 (2018).

[5] A. Manohar, V. Vijayakanth, P. Manivasagan, E.S. Jang, B. Hari, M. Gu, K.H. Kim, Investigation on the physico-chemical properties, hyperthermia and cytotoxicity study of magnesium doped manganese ferrite nanoparticles, Mater. Chem. Phys. 287 (2022), https://doi.org/10.1016/j.matchemphys.2022.126295.

[6] A. Soufi, H. Hajjaoui, R. Elmoubarki, M. Abdennouri, S. Qourzal, N. Barka, Spinel ferrites nanoparticles: synthesis methods and application in heterogeneous fenton oxidation of organic pollutants – a review, Applied Surface Science Advances 6 (2021), https://doi.org/10.1016/j.apsadv.2021.100145.

[7] J. Balavijayalakshmi, M. Saranya, Synthesis and Characterization of Copper Doped Magnesium Ferrite Nanoparticles, 2014. www.indiasciencetech.com.

[8] N. Kaur, M. Kaur, Comparative studies on impact of synthesis methods on structural and magnetic properties of magnesium ferrite nanoparticles, Processing and Application of Ceramics 8 (3) (2014) 137–143, https://doi.org/10.2298/PAC1403137K.

[9] B.M. Ali, Y.A. Alsabah, M.A. Siddig, A.A. Elbadawi, A.I. Ahmed, A.A. Mirghni, Influenced of Cu^{2+} doped on structural, morphological and optical properties of $Zn-Mg-Fe_2O_4$ ferrite prepared by sol-gel method, Adv. Nanoparticles (2020) 49–58, https://doi.org/10.4236/anp.2020.92004. *09* (02.

[10] M.A. Almessiere, Y. Slimani, S. Rehman, F.A. Khan, E.G. Polat, A. Sadaqat, S.E. Shirsath, A. Baykal, Synthesis of Dy-Y Co-substituted manganese-zinc spinel nanoferrites induced anti-bacterial and anti-cancer activities: comparison between sonochemical and sol-gel auto-combustion methods, Mater. Sci. Eng. C 116 (2020), https://doi.org/10.1016/j.msec.2020.111186.

[11] D.K. Dinkar, B. Das, R. Gopalan, B.S. Dehiya, Effects of surfactant on the structural and magnetic properties of hydrothermally synthesized NiFe2O4 nanoparticles, Mater. Chem. Phys. 218 (2018) 70–76, https://doi.org/10.1016/j.matchemphys.2018.07.020.

[12] S.K. Pradhan, S. Bid, M. Gateshki, V. Petkov, Microstructure characterization and cation distribution of nanocrystalline magnesium ferrite prepared by ball milling, Mater. Chem. Phys. 93 (1) (2005) 224–230, https://doi.org/10.1016/j.matchemphys.2005.03.017.

[13] S. Akhter, D.P. Paul, D.K. Saha, S.M. Hoque, M.A. Hakim, Structural, magnetic and electrical properties of Cu-Mg ferrites, J. Sci. Res. 6 (2) (2014) 205–215, https://doi.org/10.3329/jsr.v6i2.17351.

[14] M. Basak, M.L. Rahman, M.F. Ahmed, B. Biswas, N. Sharmin, The use of X-ray diffraction peak profile analysis to determine the structural parameters of cobalt ferrite nanoparticles using debye-scherrer, williamson-Hall, halder-wagner and size-strain plot: different precipitating agent approach, J. Alloys Compd. 895 (2022), https://doi.org/10.1016/j.jallcom.2021.162694.

[15] C. Murugesan, G. Chandrasekaran, Enhanced electrical and magnetic properties of annealed magnesium ferrite nanoparticles, J. Supercond. Nov. Magnetism 28 (12) (2015) 3607–3615, https://doi.org/10.1007/s10948-015-3198-z.

[16] M.A. Khan, M.U. Islam, M. Ishaque, I.Z. Rahman, Effect of Tb substitution on structural, magnetic and electrical properties of magnesium ferrites, Ceram. Int. 37 (7) (2011) 2519–2526, https://doi.org/10.1016/j.ceramint.2011.03.063.

[17] U. Ahmad, M. Afzia, F. Shah, B. Ismail, A. Rahim, R.A. Khan, Improved magnetic and electrical properties of transition metal doped nickel spinel ferrite nanoparticles for prospective applications, Mater. Sci. Semicond. Process. 148 (2022), https://doi.org/10.1016/j.mssp.2022.106830.

[18] A. Manikandan, J. Judith Vijaya, M. Sundararajan, C. Meganathan, L.J. Kennedy, M. Bououdina, Optical and magnetic properties of Mg-doped ZnFe2O4 nanoparticles prepared by rapid microwave combustion method, Superlattice. Microst. 64 (2013) 118–131, https://doi.org/10.1016/j.spmi.2013.09.021.

[19] M. Sivakumar, T. Takami, H. Ikuta, A. Towata, K. Yasui, T. Tuziuti, T. Kozuka, D. Bhattacharya, Y. Iida, Fabrication of zinc ferrite nanocrystals by sonochemical emulsification and evaporation: observation of magnetization and its relaxation at low temperature, J. Phys. Chem. B 110 (31) (2006) 15234–15243, https://doi.org/10.1021/jp055024c.

[20] A.C. Druc, A.M. Dumitrescu, A.I. Borhan, V. Nica, A.R. Iordan, M.N. Palamaru, Optimization of synthesis conditions and the study of magnetic and dielectric properties for MgFe2O4 ferrite, Cent. Eur. J. Chem. 11 (8) (2013) 1330–1342, https://doi.org/10.2478/s11532-013-0260-1.

[21] M. Rahman, Md Lutfor Rahman, B. Biswas, Md Farid Ahmed, Md Aftab Ali Shaikh, S. Akter Jahan, N. Sharmin, Effect of Ni-doping on coloring and photocatalytic performance of MgTi2O5 nanoceramics, J. Ind. Eng. Chem. (2023), https://doi.org/10.1016/j.jiec.2023.06.024.

[22] T. Kiseleva, V. Kabanov, A. Ilyushin, G. Markov, D. Sanga, H. Hirazawa, Structural and magnetic properties of copper substituted Mg-ferrites, in: EPJ Web of Conferences, vol.185, EDP Sciences, 2018, https://doi.org/10.1051/epjconf/201818504010.

[23] A. Balamurugan, R.S. Priya, P. Chaudhary, E.R. Kumar, T. Indumathi, C. Srinivas, B.C. Yadav, D.L. Sastry, Natural fuel assisted synthesis of Mg–Cu ferrite nanoparticles: evaluation of structural, dielectric, magnetic and humidity sensing properties, Ceram. Int. 48 (4) (2022) 4874–4885, https://doi.org/10.1016/j.ceramint.2021.11.024.

[24] L. Rajadurai, C. Sekhar Dash, S. Revathi, A. Tony Dhiwahar, M. Sundararajan, P. Ravisankar, J. Kumar Alagarasan, S. Mohandoss, R. Sambasivam, Photocatalytic degradation of tetracycline hydrochloride using pure and copper-doped magnesium ferrite nanoparticles: efficiency, kinetics and mechanism, Inorg. Chem. Commun. 162 (2024), https://doi.org/10.1016/j.inoche.2024.112197.

[25] F.H. Mulud, N.A. Dahham, I.F. Waheed, Synthesis and characterization of copper ferrite nanoparticles, in: IOP Conference Series: Materials Science and Engineering, vol.928, IOP Publishing Ltd, 2020, https://doi.org/10.1088/1757-899X/928/7/072125.

[26] M. Jafarpour, M. Rostami, S.M.H. Khalkhali, H. Nikmanesh, M.H. Majles Ara, The effect of lanthanum substitution on the structural, magnetic, and dielectric properties of nanocrystalline Mn-Ni spinel ferrite for radio frequency (RF) applications, in: Physics Letters, Section A: General, Atomic and Solid State Physics, vol.15, Elsevier B.V. September, 2022, https://doi.org/10.1016/j.physleta.2022.128285.

[27] L. Rahman, S. Bhattacharjee, S. Islam, F. Zahan, B. Biswas, N. Sharmin, A study on the preparation and characterization of maghemite (γ-Fe2O3) particles from iron-containing waste materials, Journal of Asian Ceramic Societies 8 (4) (2020) 1083–1094, https://doi.org/10.1080/21870764.2020.1812838.

[28] J. Massoudi, M. Smari, K. Nouri, E. Dhahri, K. Khirouni, S. Bertaina, L. Bessais, E.K. Hlil, Magnetic and spectroscopic properties of Ni-Zn-Al ferrite spinel: from the nanoscale to microscale, RSC Adv. 10 (57) (2020) 34556–34580, https://doi.org/10.1039/d0ra05522k.

[29] S.I. Hussein, A.S. Elkady, M.M. Rashad, A.G. Mostafa, R.M. Megahid, Structural and magnetic properties of magnesium ferrite nanoparticles prepared via EDTA-based sol-gel reaction, J. Magn. Magn Mater. 379 (2015) 9–15, https://doi.org/10.1016/j.jmmm.2014.11.079.

[30] S. Yonatan Mulushoa, N. Murali, M. Tulu Wegayehu, S.J. Margarette, K. Samatha, Influence of Cu-Cr substitution on structural, morphological, electrical and magnetic properties of magnesium ferrite, Results Phys. 8 (2018) 772–779, https://doi.org/10.1016/j.rinp.2017.12.062.

[31] Z. Hammache, A. Soukeur, S. Omeiri, B. Bellal, M. Trari, Physical and photo-electrochemical properties of MgFe2O4 prepared by sol gel route: application to the photodegradation of methylene blue, J. Mater. Sci. Mater. Electron. 30 (6) (2019) 5375–5382, https://doi.org/10.1007/s10854-019-00830-2.

[32] 25].

[33] T. Ramaprasad, R.J. Kumar, U. Naresh, M. Prakash, D. Kothandan, K.C.B. Naidu, Effect of PH value on structural and magnetic properties of CuFe2O4 nanoparticles synthesized by low temperature hydrothermal technique, Mater. Res. Express 5 (9) (2018), https://doi.org/10.1088/2053-1591/aad860.

[34] R.S. Yadav, I. Kuřitka, J. Vilcakova, J. Havlica, J. Masilko, L. Kalina, J. Tkacz, M. Hajdúchová, V. Enev, Structural, dielectric, electrical and magnetic properties of CuFe2O4 nanoparticles synthesized by honey mediated sol–gel combustion method and annealing effect, J. Mater. Sci. Mater. Electron. 28 (8) (2017) 6245–6261, https://doi.org/10.1007/s10854-016-6305-4.

[35] J. Kurian, M.J. Mathew, Structural, magnetic and mossbauer studies of magnesium ferrite nanoparticles prepared by hydrothermal method, Int. J. Nanosci. 17 (1–2) (2018), https://doi.org/10.1142/S0219581X17600018.

[36] T.F. Marinca, I. Chicinaş, O. Isnard, Structural and magnetic properties of the copper ferrite obtained by reactive milling and heat treatment, Ceram. Int. 39 (4) (2013) 4179–4186, https://doi.org/10.1016/j.ceramint.2012.10.274.

[37] M.A. Hakim, S. Akhter, D.P. Paul, S.M. Hoque, EFFECT OF Mg SUBSTITUTED ON PHYSICAL AND MAGNETIC PROPERTIES OF Cu-Mg FERRITES ARTICLE INFO ABSTRACT, Applied Research Journal 1 (2) (2015) 91–96.

[38] D. Nath, F. Singh, R. Das, X-ray diffraction analysis by williamson-Hall, halder-wagner and size-strain plot methods of CdSe nanoparticles- a comparative study, Mater. Chem. Phys. 239 (2020), https://doi.org/10.1016/j.matchemphys.2019.122021.

[39] E. Abouzir, M. Elansary, M. Belaiche, H. Jaziri, Magnetic and structural properties of single-phase Gd3+-substituted Co-Mg ferrite nanoparticles, RSC Adv. 10 (19) (2020) 11244–11256, https://doi.org/10.1039/d0ra01841d.

[40] S.K. Sen, U.C. Barman, M.S. Manir, P. Mondal, S. Dutta, M. Paul, M.A.M. Chowdhury, M.A. Hakim, X-ray peak profile analysis of pure and Dy-doped -MoO3 nanobelts using debye-scherrer, williamson-Hall and halder-wagner methods, Adv. Nat. Sci. Nanosci. Nanotechnol. 11 (2) (2020), https://doi.org/10.1088/2043-6254/ab8732.

[41] S. Singhal, S. Bhukal, J. Singh, K. Chandra, S. Bansal, Optical, X-ray diffraction, and magnetic properties of the cobalt-substituted nickel chromium ferrites (CrCo x Ni 1-x FeO 4, x = 0, 0.2, 0.4, 0.6, 0.8, 1.0) synthesized using sol-gel autocombustion method, J Nanotechnol (2011), https://doi.org/10.1155/2011/930243.

[42] M.M. Abdullah, K.H. Harbbi, X-RAY diffraction line PROFILEANALYSIS of cerium oxide nano particle by using double voigt function method 13 (20) (2018).

[43] M. Podder, M.F. Ahmed, M.R. Moni, M.L. Rahman, B. Biswas, N. Sharmin, Effect of metal ions on structural, morphological and optical properties of nano-crystallite spinel cobalt-aluminate (CoAl2O4), Arab. J. Chem. 16 (5) (2023), https://doi.org/10.1016/j.arabjc.2023.104700.

[44] Izumi, F.; Ikeda, T. Implementation of the Williamson-Hall and Halder-Wagner Methods into RIETAN-FP.

[45] K.V. Chandekar, K.M. Kant, Size-strain analysis and elastic properties of CoFe2O4 nanoplatelets by hydrothermal method, J. Mol. Struct. 1154 (2018) 418–427, https://doi.org/10.1016/j.molstruc.2017.09.104.

[46] K.V. Chandekar, B. Palanivel, F.H. Alkallas, A.B.G. Trabelsi, A. Khan, I.M. Ashraf, S. AlFaify, M. Shkir, Photocatalytic activities of Mg doped NiO NPs for degradation of methylene blue dye for harmful contaminants: a kinetics, mechanism and recyclability, J. Phys. Chem. Solid. 178 (2023), https://doi.org/10.1016/j.jpcs.2023.111345.

[47] K.V. Chandekar, M. Shkir, S. AlFaify, A structural, elastic, mechanical, spectroscopic, thermodynamic, and magnetic properties of polymer coated CoFe2O4 nanostructures for various applications, J. Mol. Struct. 1205 (2020), https://doi.org/10.1016/j.molstruc.2020.127681.

[48] K.V. Chandekar, K.M. Kant, Size-strain analysis and elastic properties of CoFe2O4 nanoplatelets by hydrothermal method, J. Mol. Struct. 1154 (2018) 418–427, https://doi.org/10.1016/j.molstruc.2017.09.104.

[49] M. Gharibshahian, M.S. Nourbakhsh, O. Mirzaee, Evaluation of the superparamagnetic and biological properties of microwave assisted synthesized Zn & Cd doped CoFe2O4 nanoparticles via pechini sol–gel method, J. Sol. Gel Sci. Technol. 85 (3) (2018) 684–692, https://doi.org/10.1007/s10971-017-4570-1.

[50] Nitika, A. Rana, V. Kumar, Evaluation of structural, magnetic, optical, electrical, and humidity sensing properties of manganese-substituted zinc ferrite nanoparticles, Appl. Phys. Mater. Sci. Process 127 (11) (2021), https://doi.org/10.1007/s00339-021-05016-4.

[51] M. Hadi, K.M. Batoo, A. Chauhan, O.M. Aldossary, R. Verma, Y. Yang, Tuning of structural, dielectric, and electronic properties of Cu doped Co–Zn ferrite nanoparticles for multilayer inductor chip applications, Magnetochemistry 7 (4) (2021), https://doi.org/10.3390/magnetochemistry7040053.

[52] J. Shah, M. Arora, L.P. Purohit, R.K. Kotnala, Significant increase in humidity sensing characteristics of praseodymium doped magnesium ferrite, Sens Actuators A Phys 167 (2) (2011) 332–337, https://doi.org/10.1016/j.sna.2011.03.010.

[53] S. Islam, Md Lutfor Rahman, Md Rassel Moni, B. Biswas, Md Farid Ahmed, N. Sharmin, Impacts of annealing temperature on microstructure, optical and electromagnetic properties of zinc ferrites nanoparticles synthesized by polymer assisted sol-gel method, Arab. J. Chem. 16 (10) (2023) 105186, https://doi.org/10.1016/j.arabjc.2023.105186.

[54] S.L. Kadam, K.K. Patankar, C.M. Kanamadi, B.K. Chougule, Electrical conduction and magnetoelectric effect in Ni0.50 Co0.50 Fe2O4 + Ba0.8 Pb 0.2TiO3 composites, Mater. Res. Bull. 39 (14–15) (2004) 2265–2272, https://doi.org/10.1016/j.materresbull.2004.07.021.

[55] R. Fieschi, A. Gafnetti, C. Ghezzi, M. Martial, D. Adler, J. Feinleib, Electrical A»d Optical Properties of Narrow-L4»d Materi, vol. 2, Il», 1959.

[56] K.V. Chandekar, S.P. Yadav, Comprehensive study of MFe2O4 (M=Co, Ni, Zn) nanostructures prepared by Co-precipitation route, J. Alloys Compd. 960 (2023), https://doi.org/10.1016/j.jallcom.2023.170838.

[57] K.V. Chandekar, S.P. Yadav, S. Chinke, M. Shkir, Impact of Co-doped NiFe2O4 (CoxNi1−xFe2O4) nanostructures prepared by Co-precipitation route on the structural, morphological, surface, and magnetic properties, J. Alloys Compd. 966 (2023), https://doi.org/10.1016/j.jallcom.2023.171556.

[58] L.C. Liu, C.C. Lai, M.T. Lu, C.H. Wu, C.M. Chen, Manufacture of biaxially-oriented polyamide 6 (BOPA6) films with high transparencies, mechanical performances, thermal resistance, and gas blocking capabilities, Mater. Sci. Eng., B 259 (2020), https://doi.org/10.1016/j.mseb.2020.114605.

[59] A.D. Volodchenkov, Y. Kodera, J.E. Garay, Synthesis of strontium ferrite/iron oxide exchange coupled nano-powders with improved energy product for rare earth free permanent magnet applications, J Mater Chem C Mater 4 (24) (2016) 5593–5601, https://doi.org/10.1039/c6tc01300g.

[60] J.K. Khan, M. Khalid, G. Mustafa, Z. Uddin, M. Saleem, A.A. Azam, Study of lanthanum ions (La3+) doped manganese-cobalt (Mn-Co) based spinel ferrite nanoparticles for technological applications, Appl. Phys. Mater. Sci. Process 128 (11) (2022), https://doi.org/10.1007/s00339-022-06106-7.

[61] M.L. Rahman, S. Rahman, B. Biswas, M.F. Ahmed, M. Rahman, N. Sharmin, Investigation of structural, morphological and magnetic properties of nanostructured strontium hexaferrite through Co-precipitation technique: impacts of annealing temperature and Fe/Sr ratio, Heliyon 9 (3) (2023) e14532, https://doi.org/10.1016/j.heliyon.2023.e14532.

[62] M. Basak, M.L. Rahman, M.F. Ahmed, B. Biswas, N. Sharmin, Calcination effect on structural, morphological and magnetic properties of nano-sized CoFe2O4 developed by a simple Co-precipitation technique, Mater. Chem. Phys. 264 (2021), https://doi.org/10.1016/j.matchemphys.2021.124442.

[63] M.J. Iqbal, M.R. Siddiquah, Electrical and magnetic properties of chromium-substituted cobalt ferrite nanomaterials, J. Alloys Compd. 453 (1–2) (2008) 513–518, https://doi.org/10.1016/j.jallcom.2007.06.105.

[64] M. Atif, M. Idrees, M. Nadeem, M. Siddique, M.W. Ashraf, Investigation on the Structural, Dielectric and Impedance Analysis of Manganese Substituted Cobalt Ferrite i.e., Co1-XMnxFe2O4 (0.0 ≤ x ≤ 0.4), RSC Adv. 6 (25) (2016) 20876–20885, https://doi.org/10.1039/c5ra20621a.

[65] A. Hosseinpour, H. Sadeghi, A. Morisako, Simulation of DC-hopping conduction in spinel ferrites using free electron gas model, J. Magn. Magn Mater. 316 (2) (2007), https://doi.org/10.1016/j.jmmm.2007.02.119. SPEC. ISS.

[66] A. Radoń, Ł. Hawełek, D. Łukowiec, J. Kubacki, P. Włodarczyk, Dielectric and electromagnetic interference shielding properties of high entropy (Zn,Fe,Ni,Mg, Cd)Fe2O4 ferrite, Sci. Rep. 9 (1) (2019), https://doi.org/10.1038/s41598-019-56586-6.

[67] E.E. Ateia, A.T. Mohamed, Improvement of the magnetic properties of magnesium nanoferrites via Co2 +/Ca2 + doping, J. Supercond. Nov. Magnetism 30 (3) (2017) 627–633, https://doi.org/10.1007/s10948-016-3839-x.

[68] K.M. Batoo, M.S.A. El-Sadek, Electrical and magnetic transport properties of Ni-Cu-Mg ferrite nanoparticles prepared by sol-gel method, J. Alloys Compd. 566 (2013) 112–119, https://doi.org/10.1016/j.jallcom.2013.02.129.

[69] R.N.P. Choudhary, D.K. Pradhan, C.M. Tirado, G.E. Bonilla, R.S. Katiyar, Effect of La substitution on structural and electrical properties of Ba(Fe2/3W1/3)O3 nanoceramics, J. Mater. Sci. 42 (17) (2007) 7423–7432, https://doi.org/10.1007/s10853-007-1835-z.

[70] P. Chavan, L.R. Naik, Investigation of energy band gap and conduction mechanism of magnesium substituted nickel ferrite nanoparticles, Physica Status Solidi (A) Applications and Materials Science 214 (9) (2017), https://doi.org/10.1002/pssa.201700077.

[71] R. Singh Yadav, I. Kuřitka, J. Vilcakova, T. Jamatia, M. Machovsky, D. Skoda, P. Urbánek, M. Masař, M. Urbánek, L. Kalina, J. Havlica, Impact of sonochemical synthesis condition on the structural and physical properties of MnFe2O4 spinel ferrite nanoparticles, Ultrason. Sonochem. 61 (2020), https://doi.org/10.1016/j.ultsonch.2019.104839.

[72] N.K. Hejazy, T.M. Hammad, Optical, Structural and Magnetic Properties of Copper-Doped Iron Ferrite Synthesized by a Sol-Gel Method * 2 (2019).

[73] A.C. Druc, A.I. Borhan, A. Diaconu, A.R. Iordan, G.G. Nedelcu, L. Leontie, M.N. Palamaru, How cobalt ions substitution changes the structure and dielectric properties of magnesium ferrite? Ceram. Int. 40 (8 PART B) (2014) 13573–13578, https://doi.org/10.1016/j.ceramint.2014.05.071.

[74] H.M. Zaki, S. Al-Heniti, A. Umar, F. Al-Marzouki, A. Abdel-Daiem, T.A. Elmosalami, H.A. Dawoud, F.S. Al-Hazmi, S.S. Ata-Allah, Magnesium-Zinc ferrite nanoparticles: effect of copper doping on the structural, electrical and magnetic properties, J. Nanosci. Nanotechnol. 13 (6) (2013) 4056–4065, https://doi.org/10.1166/jnn.2013.7434.

[75] S. Akhter, D.P. Paul, Md A. Hakim, D.K. Saha, Md Al-Mamun, A. Parveen, Synthesis, structural and physical properties of Cu_{1−X}Zn_XFe₂O₄ ferrites, Mater. Sci. Appl. 2 (11) (2011) 1675–1681, https://doi.org/10.4236/msa.2011.211223.

[76] A.C. Nawle, A.v. Humbe, M.K. Babrekar, S.S. Deshmukh, K.M. Jadhav, Deposition, characterization, magnetic and optical properties of Zn doped CuFe2O4 thin films, J. Alloys Compd. 695 (2017) 1573–1582, https://doi.org/10.1016/j.jallcom.2016.10.301.

[77] G.P. Joshi, N.S. Saxena, R. Mangal, A. Mishra, T.P. Sharma, Band gap determination of Ni-Zn ferrites, Bull. Mater. Sci. 26 (4) (2003) 387–389, https://doi.org/10.1007/BF02711181.

[78] S.K. Durrani, S. Naz, M. Mehmood, M. Nadeem, M. Siddique, Structural, impedance and mössbauer studies of magnesium ferrite synthesized via sol–gel auto-combustion process, J. Saudi Chem. Soc. 21 (8) (2017) 899–910, https://doi.org/10.1016/j.jscs.2015.12.006.

[79] M.L. Rahman, M.S. Islam, M.F. Ahmed, B. Biswas, N. Sharmin, A.J.M.T. Neger, Extraction and characterization of highly pure alumina (α, γ, and θ) polymorphs from waste beverage cans: a viable waste management approach, Arab. J. Chem. 16 (2) (2023), https://doi.org/10.1016/j.arabjc.2022.104518.

[80] K.V. Chandekar, M. Shkir, A. Khan, B.M. Al-Shehri, M.S. Hamdy, S. AlFaify, M.A. El-Toni, A. Aldalbahi, A.A. Ansari, H. Ghaithan, A facile one-pot flash combustion synthesis of La@ZnO nanoparticles and their characterizations for optoelectronic and photocatalysis applications, J. Photochem. Photobiol. Chem. 395 (2020), https://doi.org/10.1016/j.jphotochem.2020.112465.

[81] M. Shkir, K.V. Chandekar, B.M. Alshehri, A. Khan, S. AlFaify, M.S. Hamdy, A remarkable enhancement in photocatalytic activity of facilely synthesized Terbium@Zinc oxide nanoparticles by flash combustion route for optoelectronic applications, Appl. Nanosci. 10 (6) (2020) 1811–1823, https://doi.org/10.1007/s13204-019-01236-6.

[82] P. Chavan, L.R. Naik, Investigation of energy band gap and conduction mechanism of magnesium substituted nickel ferrite nanoparticles, Physica Status Solidi (A) Applications and Materials Science 214 (9) (2017), https://doi.org/10.1002/pssa.201700077.

[83] Y. Slimani, M.A. Almessiere, A.D. Korkmaz, S. Guner, H. Güngüneş, M. Sertkol, A. Manikandan, A. Yildiz, S. Akhtar, S.E. Shirsath, A. Baykal, Ni0.4Cu0.2Zn0.4TbxFe2-XO4 nanospinel ferrites: ultrasonic synthesis and physical properties, Ultrason. Sonochem. 59 (2019), https://doi.org/10.1016/j.ultsonch.2019.104757.

[84] G.R. Kumar, K.V. Kumar, Y.C. Venudhar, Synthesis, structural and magnetic properties of copper substituted nickel ferrites by sol-gel method, Mater. Sci. Appl. 3 (2) (2012) 87–91, https://doi.org/10.4236/msa.2012.32013.

[85] S.F. Mansour, S. Wageh, R. Al-Wafi, M.A. Abdo, Enhanced magnetic, dielectric properties and photocatalytic activity of doped Mg–Zn ferrite nanoparticles by virtue of Sm3+ role, J. Alloys Compd. 856 (2021), https://doi.org/10.1016/j.jallcom.2020.157437.

[86] S. Attia, N. Helaïli, Y. Bessekhouad, Y. Azoudj, M. Trari, Effect of Ni toward the optical and transport properties of the spinel solid solution NixCu1−xFe2O4 nanoparticles, J. Environ. Chem. Eng. 10 (6) (2022) 108601, https://doi.org/10.1016/j.jece.2022.108601.

[87] G. Fan, Z. Gu, L. Yang, F. Li, Nanocrystalline zinc ferrite photocatalysts formed using the colloid mill and hydrothermal technique, Chem. Eng. J. 155 (1–2) (2009) 534–541, https://doi.org/10.1016/j.cej.2009.08.008.